Soft Tactile Sensor Embedded Artificial Skin

Jianzhu Yin

A dissertation
submitted in partial fulfillment of the
requirements for the degree of

Doctor of Philosophy

University of Washington
2017

Reading Committee:
Jonathan D. Posner, Chair
Per G. Reinhall,
Joshua R. Smith.

Program Authorized to Offer Degree:
Mechanical Engineering

University of Washington

Abstract

Soft Shear Tactile Sensor Embedded Artificial Skin

Jianzhu Yin

Chair of the Supervisory Committee:

Bryan T. McMinn Endowed Associate Professor Jonathan D. Posner

Department of Mechanical Engineering

When making contact with objects, we perceive them as warm or cold, rough or smooth, and hard or soft using multiple mechanoreceptors. Current robots and prosthesis lack the perception of touch that is vital for in-hand manipulation and finger-object interaction, thus struggling on certain tasks such as slip prevention, grip control, and texture/stiffness recognition. Tactile feedback on robot manipulators and prosthetic hands are important advancement because it enables manipulation in unstructured surroundings, reveals surface/volumetric properties of objects and improves robotic/prosthetic autonomy. Sensor skin can provide rich, real-time tactile information to aid manipulation and can conformally wrap around a variety of existing fingertips. Numerous soft tactile sensors have been developed using liquid metal (eutectic Gallium Indium, or eGaIn) and flexible elastomer. These sensor skins are inferior to human tactile sensing performance in terms of sensitivity, spatial and/or temporal resolution. Current approaches to measure shear force suffer from poor resolution and ambiguity. A highly sensitive sensor skin that accurately resolves contact force in three-dimension and senses vibration is needed for artificial manipulator to better interact with the environment and external objects.

This dissertation describes the design and development of a soft tactile sensing skin that is conformable to existing robotic manipulators and provides dynamic tactile sensing of normal and shear force as well as vibration. A bioinspired shear force sensor is developed by measuring the asymmetric strain pattern of sensor skin when shear force is applied. However normal force would induce symmetric strain pattern, analytically proving that the sensor response is independent of normal force. A 2D solid mechanics steady finite element analysis is developed to evaluate the sensor performance and determine geometric parameters of the artificial skin and strain sensor that provide adequate sensitivity over the light touch shear force range. Static characterization experiments are conducted to produce the linear calibration between sensor response and shear force. This relation is matches analytical estimations as well as simulation predictions. The artificial sensor skin is further examined dynamically in stepwise unloading, slip and controlled vibration tests. We show that the sensor has potential of detecting insipient slip and can resolve vibrations equivalent, or better, than humans. The sensor resolves a variety of tactile events during pick and place, drop or handoff tasks on a robotic manipulator.

The shear tactile sensor skin is extended to two-dimensions and integrated with a normal force sensor. The resistive normal force sensor is based on deformation of liquid metal filled spiral shaped microfluidic channel with respect to normal force. The normal force sensors exhibit sensitivity of 18 %/N and better-than-human performance to measure vibration. It is shown that the integrated sensor skin encodes spatially dispersed normal force and lumped shear force in two directions, although there are design and optimization challenges to match the sensitivity to one-dimension shear sensing skin.

This research has resulted in the development of a flexible normal and shear sensing skin that is also capable of sensing vibration. The sensing skin can be applied to robotic manipulators

or prosthetic hands to improve manipulation performance, prevent slip, gather surface/volumetric object properties for autonomous robot or smarter and more user-friendly prosthesis.

Dedication

To my family for their support throughout my life.

To my girlfriend Alice Wu for her continuing love and making me a better man.

To my mentors and friends at University of Washington for the great time we had.

Acknowledgements

I owe my academic and personal development to my family, friends, colleagues and mentors. Without their support, I would not be in such privileged position to acknowledgement them here.

I would like to thank my advisor and committee chair Professor Jonathan D. Posner for the appreciation of my talent potential upon my admission and continued advisory throughout my time in graduate school. His critical thinking and passion of innovation in engineering has inspired me to grow from a fresh graduate to an experienced researcher. I had the opportunity to think and act independently and when I was stuck and seek suggestion and advisory, Prof. Posner was always there for me. Aside from academic advancement, he also gave me advice outside of the lab that benefits my character building. Here I present my sincere appreciation to Prof. Posner. I would also like to thank Prof. Veronica J. Santos for her insight from the robotics perspective. She made me realize that how much the community needs useful tactile sensors and how much impact there is from my sensor. I am grateful to Prof. Per G. Reinhall, Prof. Joshua R. Smith and Prof. Karl F. Böhringer for agreeing to present as my supervisory committee and their valuable suggestion and insight that improved the work shown here. I would also like to thank Prof. I.Y. (Steve) Shen for his advisory on vibration aspect of this work.

I would like to thank my fellow graduate students and labmates at the Posner Research Group, Jefferey Moran, Babak Moghadam, Mark Borysiak, Charlie Corredor, Karl Kerr, Andrew Bender, Jay Rutherford, Akshay Subramaniam, William Walker, Kelly Connelly, Kevin Kimura, Stefan Foulstone, Amanda Levenson and Tiffany Lo. Their assistance and fellowship during my time in the group is a valuable experience and I hereby express my gratitude.

As the love of my life, my girlfriend Alice Wu has motivated me greatly in the past years and supported me every step of the way. I cannot be thankful enough for her faith, patience and kindness with me.

The work presented below was generously supported by the National Science Foundation under Grant No. CBET-1264046. I would also like to thank UW NNIN Nanofabrication Facility for training and support in the clean room.

Finally I am grateful to all those who have made a difference in my life.

TABLE OF CONTENTS

List of Tables

List of Figures

1. Introduction

This chapter provides background information of tactile sensing using human capabilities as reference, then discusses the need of tactile sensor in the context of robotic and prosthetic manipulation application.

1.1 Significance of tactile sensing

Human beings possess the sense of touch so that we can precisely control muscle coordination during tasks such as haptic exploration and object manipulation[1]. The sense of touch is not a precisely defined term and usually categorized regarding the site of sensory inputs into haptic (kinesthetic) and tactile (cutaneous) [2]. The term haptic is widely used in the context of touch sensing where a manipulator interacts with the surroundings and resolves external object properties. Haptic sensing is related to displacement and forces of muscles, tendons and joints, while tactile sensing measures spatially resolved displacement and forces from receptors in the skin, usually at the point of contact [3]–[5]. In the example of pouring water into a glass demonstrated in Figure 1.1, sensory inputs from the finger joints that inform hand posture and position corresponds to haptic. Inputs from the skin that is in contact with the glass and jug that suggest surface properties are tactile. This work focuses on developing sensitive tactile sensing skin that can provide rich tactile information such as normal contact force, shear friction force, or vibration.

The tactile sensing capabilities of human beings enable us to explore the surroundings and deduce object surface/volumetric properties. Upon contact, we perceive an object as warm or cold, rough or smooth, and hard or soft. We can determine the object's temperatures, surface textures, mechanical properties, such as hardness, mass distribution, and geometric shapes [6].

We can also detect certain tactile events such as changing forces during a hug, incipient slip prevention, and even extract gravitational or inertial effects [7].

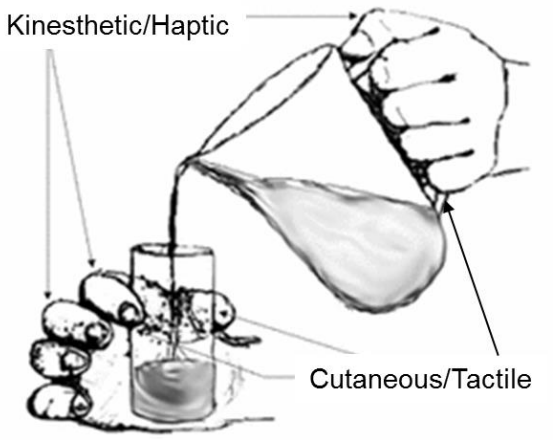

Figure 1.1 The kinesthetic/haptic and cutaneous/tactile components of human sense of touch [2]. Robotic Tactile Sensing, Chapter 3 Human Tactile Sensing, 2013, page 19-41, Dahiya, Ravinder S., Valle, Maurizio, with permission of Springer.

Tactile sensing can be categorized into a few modalities. Normal force sensing is vital in grasp force control, contact location detection and edge detection. Humans regulate grasp force to be 1.2-2 times the minimum force required without slip [8], [9], which enables holding delicate objects without dropping or damaging them. When the skin is pressed against an object edge, static force mechanoreceptors surrounding the edge respond and resolve the edge with high spatial resolution[10]. Upon contact both normal and shear forces are present and shear force sensing is critical to provide the information of friction in slip detection [11]. It is also of importance in the grasp force regulation in that it reveals the dynamic features of the manipulating object such as slip, rotation, surface friction and inertia [12], [13]. There are also evidence suggesting that the combination of normal and shear force yields surface texture [14].

Vibration sensing is thought to contribute to texture recognition and incipient slip detection [6], [15]–[17]. Tactile perception of fine texture as small as a few microns is resolved by vibrations generated while the finger is scanning the surface [17]–[19].

The majority of the tactile sensing in humans occurs in the hand. The skin of a human hand is well-equipped to resolve tactile information spatially and temporally. Human fingertips are equipped with mechanoreceptors to collect tactile information [1]. There are 17,000 mechanoreceptors in the skin of a human hand. The receptors can be categorized into four groups. [20] Figure 1.2 shows the layout of mechanoreceptors in glabrous (hairless) skin and Table 1.1 shows their specifications. They are categorized by receptive field size and temporal adaptivity. Type 1 afferents (sensory nerve fiber) corresponds to small receptive fields and type 2 to large fields. Rapid adapting (RA) type afferents stop responding to continuous static stimulus after a short amount of time and hence considered measuring dynamic forces. Slow adapting (SA) afferents continuously respond to static forces. Pacinian corpuscles are extremely sensitive, detecting 10 nm of displacement at best [21]. They have lower spatial resolution and high sensitivity at around 250 Hz, thus primarily considered as vibration sensors as the low-frequency stimuli is filtered out [22], [23]. Ruffini corpuscles are sensitive to skin stretch and deformation [24], detecting contact force directions and finger conformation [1], [25], [26]. Merkel's disks are densely populated at the human fingertip (~100 per cm^2) and they perceive edge and curvature with great spatial resolution of 0.5 mm [22]. Meissner corpuscles are known to be responsible for low frequency skin motion [21]. Hence it is believed that they inform incipient slip and provide feedback for grip control [22].

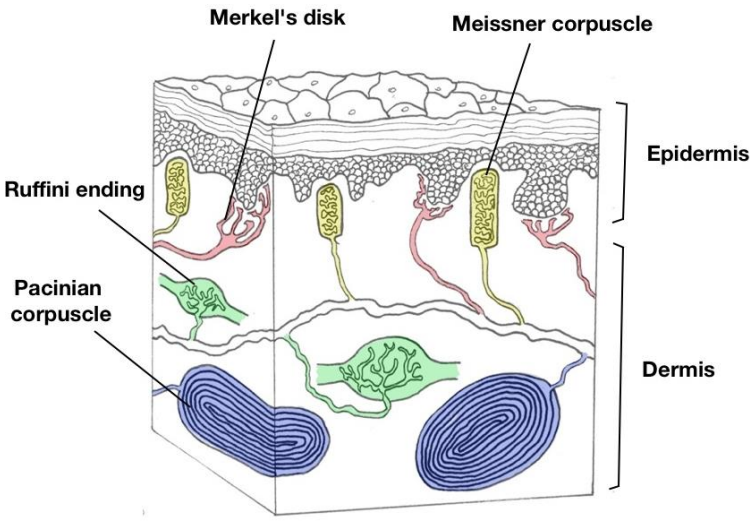

Figure 1.2 Four kinds of mechanoreceptor in glabrous skin. Merkel's disk and Meissner corpuscle are located superficially in epidermis. Ruffini ending and Pacinian corpuscle are deeper in the dermis [27].

Table 1.1 Classification of four mechanoreceptors based on their specification and stimuli features [6], [28], [29].

Classification Basis	Pacinian Corpuscle	Ruffini Corpuscle	Merkel's Disk	Meissner's Corpuscle
Type	RA II	SA II	SA I	RA I
Spatial resolution [mm]	10+	7+	0.5	3-4
Vibration threshold [μm]	0.01	40	8	2
Stimuli Frequency [Hz]	40-800	0.4-100	0.4-3	3-40
Sensory Function	High frequency vibration detection	Stable grasp, tangential force	Curvature and edge detection, spatial discrimination	Low frequency motion detection, grip control.

Human beings rely on the tactile sensing feedback in various manipulation tasks. Tactile information enables humans to deduce certain object properties that cannot be inferred from other modes of sensing such as vision [6], [16]–[19]. It has been shown that with visual feedback only, human operators tend to exert much more gripping force than needed [30]. In the example of picking up an egg, multiple modes of tactile sensing participate during different stages of the task. Upon contact Pacinian corpuscles over the finger and Meissner's corpuscle at the contact

location will respond, indicating contact. As the contact force stabilizes, Ruffini corpuscles and Merkel's disks report contact forces and regulates the grip. The static forces and indentation can suggest the egg's hardness and weight. As the person rests the egg on his/her palm and slides a finger on the surface of the egg, roughness can be felt with Pacinian corpuscles' response. The egg's shape and cracks can be perceived using Merkel's disks' response. Finally, the egg is placed on a surface and again Pacinian corpuscles report the contact, with other mechanoreceptors indicating the release of the grip. This example provides a description of how tactile sensing is relevant in tasks of manipulation and important forming the sense of touch that constructs part of our perception to the surrounding world and external objects.

1.2 Tactile sensing in robotic and prosthetic applications

Robot manipulation and human prosthetic hands are important for a variety of reasons. Robotic and prosthetic manipulation with visual perception has shown to be successful in controlled environments. For example, optically controlled robots can aid in the construction of automobiles in engineered and tightly controlled assembly lines. However, the need for precise robot manipulation in applications with unstructured environment are growing [31], [32]. Surgical robots have to precisely distinguish different tissues from their texture and stiffness similar to an experienced surgeon [11], [31]. Prosthetic hands restore appearance and function of the lost body part and the demand is pressing since it is estimated that 41,000 persons in the United States undergo an upper-limb amputation in 2005 [33], [34]. Prostheses have been shown to be helpful in daily activities including hygiene, eating, grooming and dressing yet they are challenging to use [35]. Further technical advancement of prosthetic hands is required to improve prosthetic acceptance and quality of life for a wide range of manipulation tasks including manipulating an egg or glassware without crushing or slipping, locating and identifying objects

such as a remote control in the dark or a key in the pocket when vision input is hindered [36], [37].

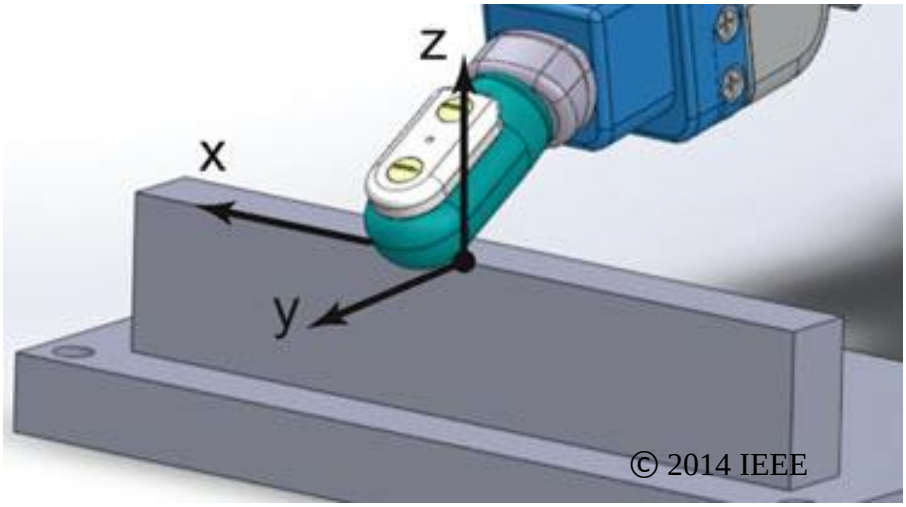

Figure 1.3 Demonstration of edge detection of a robotic fingertip in haptic exploratory motion [38]. Stroke motion in *x*,*y* and *z* direction individually and combined has been implemented. Estimated edge orientation has a RMS of 5 degrees with respect to the true value.

Tactile feedback is a promising answer to these challenges because it enables precise manipulation such as minimal access surgery and tele-operation in complex environments, reveals surface/volumetric properties of objects, and increases robotic/prosthetic autonomy, such as reflexes [11], [28], [31], [39]. At the beginning of a manipulation, the robot/prosthesis needs to know if and when the object is in contact. Low resolution and often blocked visual information is insufficient without tactile information from contact [40]. During the manipulation, the geometric shape, surface roughness and stiffness of the object can be obtained through tactile sensing, which can be used to construct a well-defined object model and enhance precise manipulation [14], [40]–[42]. Grasp forces are monitored and regulated through tactile sensing and slip is prevented by dynamic sensing [43]. Overloading the end effector is also of concern for both the robot system and the manipulating object without tactile feedback,

especially in rigid link mechanisms [31]. Failure to measure and exert appropriate amount of force could lead to damage of the manipulating object and/or the end effector itself.

Tactile sensing modalities relating to pressure and strain are typically categorized into normal, shear and vibration sensing, of which all are important tactile sensing capabilities for highly functioning robotic and prosthetic manipulation for applications such as slip detection and texture recognition [44].. Vibration sensing is typically discussed separately because the signal frequency is usually up to 1 kHz, although dynamic measurement of either normal or shear direction displacement falls into this category. Object compliance characterization and grip control can be performed by monitoring contact forces of normal and shear forces [45], [46]. Slip can be detected using friction-cone monitoring taking dynamic normal and shear force as input, bandpass filtering using vibration related measurements, or learning algorithm that utilize all tactile feedback [47]. Vibration measurements can reveal surface properties and indicate critical dynamic tactile events during incipient slip, lateral sliding, light tap and clicking [6], [15]–[17]. Artificial manipulators can distinguish surface texture similar to human using vibration tactile feedback [15].

Spatially and temporally resolved normal and shear stresses are critical mechanical measurements that need to be resolved on artificial fingertips. Sensor design criteria are typically task-specific; however, general sensor specifications can be guided by physiological properties of human mechanoreceptors and summarized in Table 1.2 [39], [48]. Within the scope of in-hand manipulation, normal and shear forces up to 10 N should be resolved with an optimal dynamic range of 1000 [39]. A normal force spatial resolution of 1.25 mm has been suggested to properly resolve object geometric features [6], [28], [39]. It is less clear how well shear forces need to be spatially resolved, spurring further research of desired resolution during in-hand manipulation.

Low latency temporal response contributes to better control stability, faster reflex-like responses, and can enable inference of surface properties such as roughness, shape, or coefficient of friction during haptic exploratory motion [15], [44], [49]–[51]. Humans can detect vibrations as high as 700 Hz although frequencies such as 100 Hz, 250 Hz or 1000 Hz have been proposed for vibration sensors for specific applications [6], [28], [39], [40], [43].

Table 1.2 Design guidelines for tactile sensors in the context of in-hand manipulation [39], [43].

Metrics	Normal and Shear	Vibration
Sensitivity	0.01 [N]	1-10 [μm]
Dynamic range	1000	
Sensing frequency [Hz]	0-32	~250
Spatial resolution [mm]	Normal: 1-2 Shear: Not clear	10-1000
Linearity/hysteresis	Repeatable and monotonic	
Robustness	Immune to EMI, chemically inert, mechanically flexible and compliant.	
Integration	Low power consumption.	

The tactile sensors developed over the past three decades have not yet met the tactile sensing needs of the robotic and prosthetic hands community. The first tactile sensors developed are MEMS (microelectromechanical system) tactile sensors constructed from rigid materials such as gold, aluminum, chromium, silicon and indium tin oxide (ITO) [52]–[55]. Sohgawa *et al.* used an array of groups of 4 cantilever structures to resolve normal and shear stress [52]. These cantilever structures are made from Au, Cr, Si, SiN, SiO_2 and placed on silicon wafer. Muhammad *et al.* developed a capacitive normal force sensor using n+ Si diaphragm and showed

potential of distinguishing texture while sliding the sensor against different surfaces [53], [54]. Wisitsoraat *et al*. used ITO as piezoresistor and developed a MEMS normal force sensor [55]. While being sensitive and well-developed, rigid MEMS sensors are intrinsically incompatible with the requirement of flexibility, conformability and robustness. Soft skin conforms to the object and hence able to provide contour information or increase grasp stability [28], [56]. Despite the effort to integrate such sensors in flexible elastomers [57]–[59], they are found to fail at repeated strain at a few percent [60]–[62].

In order to resolve normal and shear forces as well as vibration in the restricted space on an artificial fingertip, a wide variety of soft tactile sensors have been demonstrated including whole finger sensors [15], [16], [45], [47], [63], [64] and artificial skin based sensors that are compatible with existing robotic and prosthetic hand actuators [65]–[68]. Soft, multimodal, whole finger sensors that use finger deformation related fluid impedance measurement to detect normal and shear forces up to 100 Hz and piezo-resistive pressure transducer to measure vibration up to 2200 Hz have been successful in determining object compliance, detecting slip and distinguishing texture [15], [46], [47], [64]. This whole finger sensor can measure shear force range up to 6 N with an average uncertainty of $\pm$0.6 N [45], [46], and its frequency sensitivity is better than that of humans up to 1 kHz [15], [16]. A robot hand equipped with the fingertip has shown to be able to perceive local shape, which could be used to advance robot autonomy and provide haptic feedback to human teleoperators [63]. Numerous sensors and algorithms have been developed to detect and avoid slip [69]. Su *et al*. presented a grip force controller that could pick up objects of varying mass and texture [45]. The controller utilized tactile information to detect insipient slip and increase grip force to avoid further slippage. Chitta *et al*. estimated the internal state of the object using a mobile manipulator equipped with temporal resolved force

information [70]. The robot was able to distinguish open bottles from closed ones and if there is content inside. They were also able to detect the motion of liquids in the bottle using high frequency component of the tactile information. Another whole finger tactile sensor using accelerometer placed adjacent to contact in the artificial finger detected vibration signal of up to 1 kHz during sliding motion [44]. Work on robust whole finger sensors have collectively demonstrated the capabilities of multimodal tactile sensing of both static and dynamic signals, yet whole finger sensors do require modification of manipulator end effectors which may limit the available effector design space such as material, weight, shape. It also hinders integration of additional sensing modalities such as proximity or temperature.

Sensor skins that can be wrapped conformally around robotic manipulators minimize the need for modification of the end effector, more closely mimicking biological systems. Miniaturized soft MEMS sensor skins arrays of different insulator and conductor materials have been developed [67], [68], [71]–[75]. Typical soft insulator materials are silicones and polymide [76]. Polydimethylsiloxane (PDMS) based sensors have been demonstrated as robust, non-toxic, highly flexible, low cost, and have simple processing techniques [65], [71], [77], [78]. Some other sensors are also developed from Ecoflex elastomer [71]–[75]. Aluminum and copper have been used to construct conductor in some sensors, yet these still face challenges of solid state materials such as fatigue and failure at high strain that is inevitable in soft skin [52], [57]–[60], [76], [79]. Soft conductor materials include conductive elastomer and liquid metal. Conductive fillings such as carbon black[80], [81], carbon nanotube[80], [82], graphene[83] or silver[84] can be added to elastomer to construct conductor. Polymer conductors have been limited by low conductivity to effectively compose leads or capacitor plates. A recent approach to develop flexible artificial skin is to use liquid-metal-based transducer embedded in elastomers. These

materials hold potential to construct flexible tactile sensor that translates mechanical stimuli to electrical signals. Liquid metal filled channels are intrinsically immune to cracks and fatigue, suitable for conformal wrapping and repetitive, large strains. EGaIn is a conductive liquid metal at room temperature and can form microstructures with a 2 μm spatial resolution by injection into micro-channels [65], [71]–[75], [85]. EGaIn traces that are 200~300 μm wide can be rapidly patterned by microcontact printing, 3D printing, or stencil lithography [86]–[89]. A number of artificial skin based sensors that are compatible with existing robotic and prosthetic hand actuators are presented [65]–[68].

A capacitive sensor is usually composed of two flat-plate electrodes with dielectric material in between and benefits from high sensitivity, ease of building an array, and high special resolution [57]–[59], [65], [72], [81], [90]. Arrays of capacitive sensors can be used to generate normal force sensors with 1 mm spatial resolution or infer shear deformation [58], [65]. However, they are also susceptible to EMI interference, crosstalk, and parasitic capacitance. Ponce Wong *et al*. demonstrated a microfluidic normal force sensor with a 5 by 5 array of deformable parallel plate capacitors and calibrated from 0 to 2.5 N [65]. Roberts *et al*. presented a soft-matter sensor that used multiple taxels and wired parallel plate capacitors differentially to detect shear deformation in 2D [72]. Weigel *et al*. designed a skin-worn touch sensor that distinguishes light and firm touch [91].

Resistive sensors, including strain gauges and piezoresistive sensors, convert deformation to change in electrical resistance, which can be easily measured by 4-wire sensing or a Wheatstone bridge circuit [52], [68], [71], [73], [75], [76], [78], [82], [83], [92]–[95]. They generally have good sensitivity over a large sensing range, high scanning rate and easy to design and implement. Their weaknesses include lower repeatability, high power consumption, and

sensitivity to temperature. Park *et al*. presented an artificial skin capable of measuring uniaxial strain in three directions constructed with serpentine and spiral eGaIn channels that could detect pressure starting from 15 kPa, which is not sufficient for light touch applications [75]. Majidi *et al*. showed a centimeter-scale, non-differential soft curvature sensor [74].

Other sensing transduction principles use piezoelectric [96]–[99], inductive [100]–[102], or optical effects [103]–[108]. Piezoelectric sensors generally have good high-frequency response and are good candidates for vibration sensors [39]; however, they can only sense dynamic forces, and their temperature sensitivity is a significant concern for applications [28]. A number of vibration sensors have been developed to aid perception of texture and detect precursors of slip [109]–[114]. Majority of these sensors are constructed with piezoelectric materials such as lead zirconate titanate (PZT) or polyvinylidene fluoride (PVDF). PVDF is preferred because of its flexibility, large piezoelectric coefficients and chemical inertness [43]. Presented as a standalone sensor integrated in the fingertip [114], [115], these vibration sensors are seldom integrated with other sensing modalities and there are fabrication limitations to expand the application to the entire hand [43]. Inductive sensors benefits from high dynamic range, but suffers from large size and low repeatability [39]. Optical tactile sensors are generally immune to low frequency EMI and have high spatial resolution [28]; however, rigid and large components have hindered its application [39].

Table 1.3 Specification of recent soft tactile sensors and proposed specification of the shear sensing skin in this work. "N" in parenthesis stands for normal force sensor, "S" stands for shear force sensor.

	Size Conformability on Fingertip	Normal or Shear?	Force detection threshold [N]	Force precision [N]	Force range [N]	Vibration (~250 Hz)
Park *et al.*, IEEE Sensors Journal, 2012	No	Normal only	1.8	0.16	0-7.9	No
Ponce Wong *et al.*, Sensors and Actuators A: Physical, 2012	Yes	Normal only	~0.1	0.18	0-2.5	No
Vogt *et al.*, IEEE Sensors Journal, 2013	No	Normal and Shear	1 (N) 0.2 (S)	0.2 (N) 0.2 (S)	0-5 (N) 0-1 (S)	No
Roberts *et al.*, 2013 IEEE ICRA	No	Normal and Shear	0.4 (N) 0.25 [mm] (S)	2 (N) 0.25 [mm] (S)	0-10 (N) 0-3 [mm] (S)	No
Hammond, IEEE Sensors Journal, 2014	Yes	Normal only	0.05	0.01	0-0.25	No
Charalambides *et al.*, J. Micromech. Microeng., 2015	No	Normal and Shear	0.05	0.5 (N) 0.05 (S)	0-4 (N) 0-1.5 (S)	No

Table 1.3 shows the specifications of recent soft tactile sensors with regards to size, sensitivity, and sensing modality. To date, no artificial skin has matched the flexibility, sensitivity, and dynamic range of human skin [39], [116], [117]. Not all of these sensors fit on the constrained geometry space that has the size of a human fingertip. Some integrated normal and shear force sensing units have sensing ranges of 0.3-8 N according to their target application

[11], [28], [40], [43]. Sensor skins have demonstrated the capability to spatially resolve normal force over large surface area [59], [71], [73], [75], [76], [90] with spatial resolution consistent with human hands [58], [59], [65]. However, to our knowledge none tactile skin sensor has reported vibration sensing capability.

There are only a few strategies to measure shear force, such as pairs of planar strain gauges [95], vertical cantilevers[92], or clusters of normal force taxels, where they are strategically positioned in pairs or quadruples such that shear force acting at the center of the sensor cluster results in unique combinations of normal force readings [58], [72], [73], [81]. Vertical cantilevers method is difficult to implement with soft flexible materials. For the strategy using clusters of normal force sensors, the sensitivity can be enhanced by adding a bump or ridge at the center on the surface, similar to a human's fingerprint, or adding rigid force-post embedded in the media over the sensing elements [58], [72], [73]. While the integration of normal and shear sensing modalities is simple and easy to develop, this approach could suffer from reduced spatial resolution since it takes several taxels to construct a single sensing unit and requires sensor coverage throughout all possible point of contact. Considering pairs of strain gauge or a cluster of normal force sensors, an incorrect shear force can be resolved from non-uniform normal force only. In robotic applications, the location of contact is arbitrary which would necessitate a large number of distributed sensors. Tactile sensors that resolve shear forces away from the point of contact may be beneficial, especially when faced with constraints on space, such as the small region of a fingerpad. Sensing modalities that do not require localized sensing for direct measurement of stimuli can be displaced to make room for other sensing modalities, such as normal force or temperature.

In summary, a variety of tactile sensors have been developed ranging from rigid MEMS sensor to whole finger sensors and flexible tactile sensing skin. Despite the sensor development the gold standard of human tactile sensing capabilities hasn't been reached. While some sensors are outstanding in a few performance metrics and requirements, the specifications listed in Table 1.2 haven't been met in an integrated way. A useful tactile sensor has to be flexible under large strain and conformable to existing robotic manipulators. In particular, soft sensor designs that produce reliable shear force measurement and address vibration sensing modalities are scarce. A sensitive flexible shear tactile sensor that conforms and integrates into existing fingertips that also measures vibration hasn't been presented. A sensor that meets multiple design criteria and constraints shall be a useful tool for robotics and prosthetics applications ..

In this work, we develop bioinspired, thin and flexible liquid metal filled resistive PDMS microchannel based shear force sensor skin. The sensor skin is wrapped around a finger-shaped effector and fixed at the location of the nail bed. When the skin is subjected to shear force, regardless of the location of contact, it results in one side of the skin in tension and the other side in compression that buckles and bulges similar to a human fingertip. The tension and compression are measured by embedded liquid metal filled resistive microchannel strain gauges that are strategically placed adjacent to the nail bed. We present the sensor design, finite element analysis (FEA) model static mechanical characterization, as well as static and dynamic response experiments. The resistive shear sensing skin is shown to be sensitive, precise, capable of capturing dynamic tactile events, and on par with human vibration sensing capabilities. The resistive shear sensing skin is intrinsically flexible and immune to fatigue or other problems of solid-state sensors when subjected to repeated large strain. I also design, fabricate, and evaluate an integrated sensing skin solution that measures two dimensions of shear force, spatially

resolved normal force, and vibration sensing in the normal and shear force directions. The normal force sensor is based on channel deformation induced resistance change with respect to normal force. Park *et al.* demonstrated this idea with a spiral shaped sensor of approximately 20 mm in diameter and 1 mm in channel width and height [71]. In this work, we reduce the sensor size consistent with the size constraints of a fingertip. Here, the normal force sensor diameter is 3 mm and channel width is 50 μm, allowing a total of eight normal force sensing taxels on the finger pad.

2. Theory of Operation of Shear Sensor Skin

The shear sensing skin design is inspired by the layered structure of the human fingertip. Skin consists of epidermis (outermost layer), dermis, and subcutaneous fat tissue. While all of these layers are soft relative to the underlying bone, the subcutaneous fat tissue is much softer than the epidermis and dermis, thus, skin tends to shear and slide with respect to the underlying bone when shear force is applied to the finger pad. This deformation results in tension on one side of the fingerpad and compression on the other side. We can resolve shear force by leveraging the asymmetry in the strain that occurs across the fingerpad, provided there is little to no Poisson's effect at the shear sensing taxels. The Poisson's effect is negligible when normal forces are not applied directly to the shear force sensing taxels.

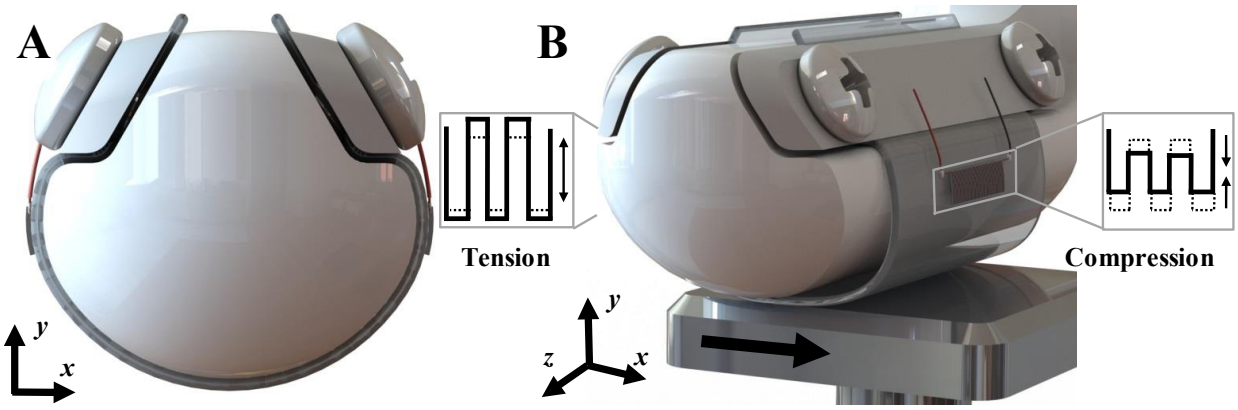

Figure 2.1 Schematics of the resistive shear sensing skin design and theory of operation. (A) The artificial skin is conformally wrapped around a rigid fingertip and affixed using mounting brackets that mimic the region of nail bed attachment on a human finger. The eGaIn-filled microchannel strain gauges are located on the radial and ulnar aspects of the finger. (B) A rigid plate applies a shear stress that drives the skin to slide relative to the rigid finger and results in the opposing sides of the sensor skin to compress (buckle) and stretch. The difference in resistance between the two opposing strain gauges is used to measure the shear applied shear force.

Figure 2.1 shows a schematic of the resistive shear sensing skin and mode of operating. The sensor skin wraps around a rigid artificial fingertip and is fixed with two mounting brackets near the top of the finger at a location proximal to the perimeter of a human finger nail bed, as shown in Figure 2.1A. The eGaIn filled microchannel strain gauges are located in the skin, adjacent to the fixed mounting brackets. The interface between the rigid fingertip and flexible skin is lubricated so that the skin can slide. When the skin is subject to shear force at the location of fingerpad, as shown in Figure 2.1B, it slides relative to the rigid finger at the point of contact putting the fore and aft sides of the sensor skin in compression (buckling) and tension, respectively. The asymmetric strain pattern allows us to uniquely correlate the difference between the strains to the amount of shear force applied on the fingertip. This shear sensing skin is designed for inherent compatibility to a wide variety of artificial fingertips.

The strain gauge sensor microchannel design is a compromise between signal to noise ratio, power consumption, and microfabrication constraints. Considering *N* strips each of length *L* forming a strain gauge with total width *W*, the total length of the conductor consists of *NL* in the longitudinal direction and *W* in the transverse direction. Since $N \gg 1$, the transverse part can be ignored and the total resistance is approximately $\rho NL/(wh)$. The resistance change is proportional to longitudinal deformation. The power consumption of the strain gauge is $V^2/R = V^2wh/\rho NL$ where V is the applied voltage. The measured resistance change can be related to strain using the gauge factor $F = \Delta R/R_0\ /\varepsilon$, where ΔR is the change of resistance, R_0 is the resistance at the un-deformed state, and ε is the strain. A uniaxial tensile stress with linear elasticity at small strain yields, $\frac{\Delta R}{R_0} = \frac{1+\varepsilon}{(1-\upsilon\varepsilon)^2} - 1 \approx (1 + 2\upsilon)\varepsilon$ where υ is Poisson's ratio of the material. The Poisson's ratio of an incompressible elastomer is 0.5 which results in a gauge factor of PDMS encapsulated liquid metal gauge is estimated at $(1 + 2\upsilon) = 2$. These equations

show that it is advantageous to maximize the sensor resistance because it minimizes the sensor power consumption and results in greater measured sensor response. Large sensor resistance can be achieved with small channel cross-section dimensions; however, there is a practical limit to the minimum channel cross-section dimensions because larger filling pressures and better sealing techniques are required to fill the channels with liquid metal as microchannel dimensions become smaller. In this work, we compromise these design constraints with 50 μm width and height and an approximately 210 mm long serpentine channel made of N = 70 strips that are L = 3 mm long. The calculated nominal resistance of each strain gauge is approximately 25 Ω, which is verified in experiments.

In this study, the gauge factor is experimentally determined by a tensile test, where a microfluidic strain gauge is uniaxially loaded with controlled strain. The strain gauge-encapsulated PDMS strip is fastened to a linear stage (443, Newport, Irvine, CA, USA) and actuated manually with a Vernier micrometer (SM-50, Newport, Irvine, CA, USA). Figure 2.2 shows the relationship between normalized sensor response as $\widetilde{\Delta R} = \Delta R/R_0$ and strain for six independent trials. The gauge factor value is determined as 1.62, from the slope of this plot using linear regression analysis. Kramer *et al.* measured a gauge factor of 1.5 using a similar PDMS material and trace width [118]. The small discrepancy between these measurements may have resulted from differences in strain ranges and PDMS curing method. Only data under 0.2 strain is considered in this work while Kramer *et al*. fitted data under 0.5 strain. In this work, PDMS material is cured at 80 ℃ for 1 hour while Kramer *et al.* used 60 ℃ for 2 hours.

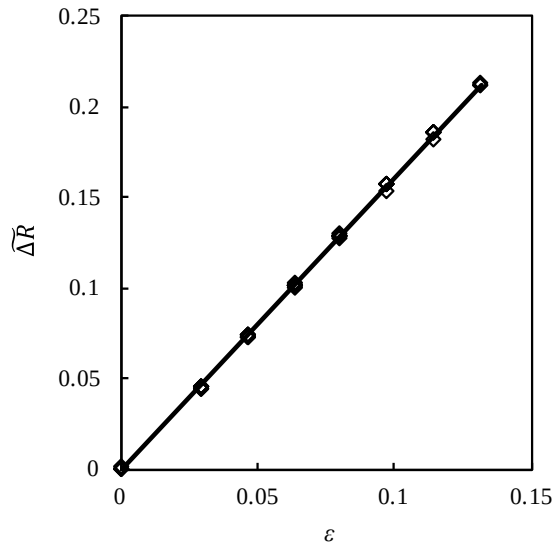

Figure 2.2 Relationship between the normalized change of strain gauge resistance and strain up to 15%. The gauge factor is determined as the slope of the linear regression between the two variables.

3. Numerical Simulation of Shear Sensor Skin

We developed steady, two-dimensional finite element solid mechanics models (COMSOL Multiphysics, Boston, MA) with linear elasticity to predict the sensor response to various normal and shear force loading conditions. We used these models to determine the appropriate placement of the strain gauges to obtain linear, high sensitivity sensor response that is independent of the applied normal force. The model was composed of two domains: one for the rigid fingertip core and one for the PDMS artificial skin. Young's modulus and Poisson's ratio of the fingertip were set to be 3.2 GPa and 0.3, respectively, in order to represent a rigid plastic material such as acrylic. We assumed the PDMS skin was uniformly linear elastic and incompressible with a Young's modulus of 1.292 MPa and a Poisson's ratio of 0.5 (0.49 to avoid numerical difficulties).

The mechanical properties of the PDMS material were determined experimentally by an electromechanical universal test machine (5585H, Instron, Norwood, MA USA). We prepared PDMS in the same way as in the device fabrication. The specimens were formed into a type C dogbone in accordance with the ASTM D412 standard. Figure 3.1 shows the stress-strain relationship for strains under 20% for seven independent tensile tests on two specimens. The Young's modulus of the PDMS was found to be 1.29 MPa through linear regression of the stress-strain curve for strains under 5%. It was in close proximity with 1.53 MPa reported by Schneider *et al*. [77], who measured the same PDMS product for five samples. The difference in measured stiffness is likely due to the fact that our PDMS samples were cured at a lower temperature than that used by Schneider *et al*. It is known that the stiffness of the PDMS increases at higher curing temperatures. [119]

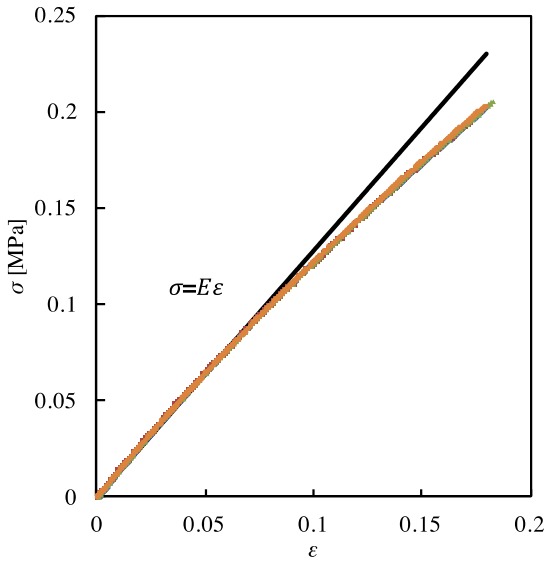

Figure 3.1 Stress-strain relationship of RTV 615 PDMS under tensile test with strain less than 0.2. Seven data sets are plotted, but they overlap one another closely. The black solid line is the linear estimation for strain under 5%.

Linear elasticity was used to describe the stress-strain relation at the strain levels considered in the model. Throughout the modelling study, the maximum strain level was 9% and the true stress deviated from the linear estimation by less than 5.5%. A hyperelastic model, such as Mooney-Rivlin, would be more accurate for describing strain softening at high loads; however, linear elasticity at lower loads is sufficient to validate the design and provide general guidelines for selecting sensor parameters such as spatial location, gauge size, channel dimension, etc.

We assumed that the strain gauges would not alter the PDMS material stiffness. The boundaries where the artificial skin was fastened to the fingernail were specified as fixed. The boundaries between the rigid fingertip and flexible PDMS skin were designated as non-penetrable contact. The skin can slide relative to the fingertip with a static Coulomb friction

coefficient of 0.04 that was determined from experiments where a strip of PDMS was pulled horizontally until slip occurred relative to a lubricated acrylic surface. The normal force was actuated by a known weight, and the horizontal friction force was recorded by a 6-axis force/torque transducer (Nano 17, ATI, Apex, NC). A linear regression analysis was performed and the slope, representing the static coefficient of friction, was estimated to be 0.04 from three independent trials. The nonzero y-intercept of the linear regression line was attributed to surface adhesion and was modeled in the numerical simulation accordingly.

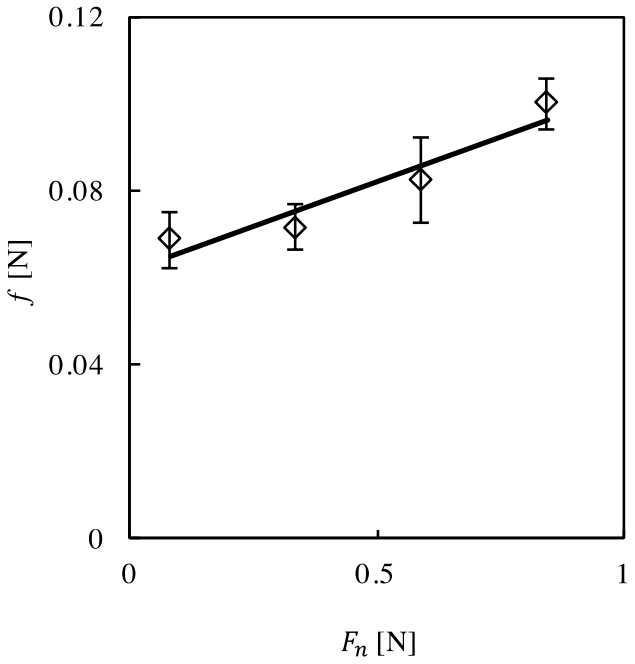

Figure 3.2 Friction force at various normal force levels between the PDMS and lubricated acrylic surface. Slope of linear regression is characterized as coefficient of friction.

The contact between the skin and stimulus (object contacting the fingertip) was not considered because, according to Saint-Venant's Principle, the sensor response is equivalent to

that of a uniform boundary load at the contact location as long as the contact is sufficiently far from the sensor location. Since the friction force between the skin and rigid fingertip is path-dependent, the loads in both normal and shear direction in the model were applied in the same order as the experiments. The normal force is first applied and shear force increases from zero to the value of normal force in 0.1 N increments. Four cases were examined where normal forces are 0.5 N, 1 N, 1.5 N, and 2 N.

The rigid fingertip core was meshed with free triangular elements and the PDMS skin with mapped quadrilateral mesh elements. The maximum element size in the skin domain was set at 0.14 mm. The total number of elements was 1648 and minimum quality was 0.85 [120]–[122]. Further mesh refinement did not alter the results, suggesting that the mesh was sufficiently resolved. In post-processing, the strain in the circumferential direction was evaluated to strategically place the strain gauges in the location that yielded linear response, largest sensitivity, and independence to applied normal force at the bottom of the fingertip. The normalized sensor response was defined as,

$$\widetilde{\Delta R} = \Delta R_1/R_{1,0} - \Delta R_2/R_{2,0} = F(\varepsilon_1 - \varepsilon_2),$$

where $R_{1,0}$ and $R_{2,0}$ are radial and ulnar strain gauge resistances when there is zero load, ΔR_1 and $\Delta \mathrm{R}_2$ are changes of resistances with respect to $R_{1,0}$ and $R_{2,0}$, respectively, and ε_1 and ε_2 are surface averaged tangential strain at the strain gauge locations, respectively. The normalized sensor response was calculated and plotted against shear force at different normal force levels.

The simulation results are drawn from cases with four normal forces: 0.5 N, 1 N, 1.5 N and 2 N. In each case, the normal force is applied first and shear force increases from zero in increment of 0.1 N. Figure 3.3 shows the strain distribution contour with a 1 N normal force and

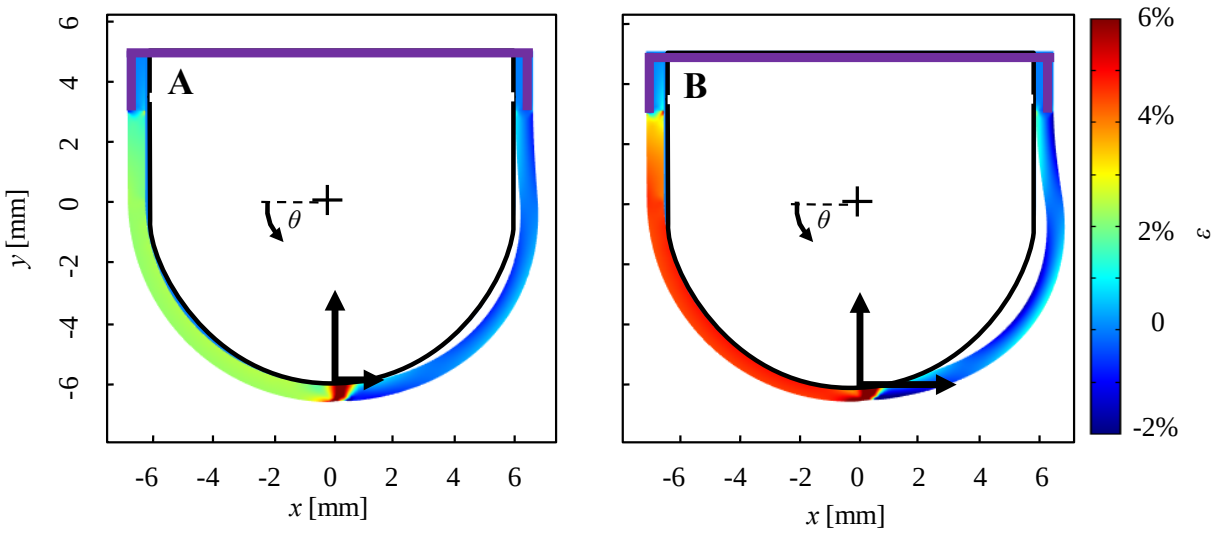

Figure 3.3 Circumferential strain distribution contour with normal force F_n and shear forces F_t. (A) and (B) show skin strain for F_n=1.0 N with F_t=0.5 N and F_t=1.0 N, respectively. The external force, whose normal and tangential components are shown as bold arrows, is applied at the bottom center of the sensor skin at (0,-6.35). The color legend shows the circumferential strain scale with positive and negative values corresponding to tensile and compressive strain, respectively. The purple lines show the fixed boundaries. The shear sensing skin is divided into regions of circumferential tensile and compressive strain, with compression and buckling occurring on the side of the finger to which the shear force vector head points. The magnitude of tensile strain is significantly higher than compressive strain, and is a strong function of shear force.

shear forces 0.5 and 1 N. In each case, the normal force was applied first and then the shear force was increased from zero in increments of 0.1 N. In both cases, a circumferential tensile strain develops on the tail-side of the shear force vector (-x direction in Figure 2.1) while a circumferential compressive strain develops on the head-side of the shear force vector (+x direction in Figure 2.1). The magnitude of tensile strain is larger than that of compressive strain due to buckling of the compressed region of the sensor skin. The stretching and compression of

the sensor skin is asymmetric, resulting in an overall increase in skin length that results in a separation of the sensor from the rigid core, that is analogous to a bulging finger pad under significant shear stress. A large magnitude tensile strain forms at the location that the normal force is applied (0,-6.35) due to Poisson's effect.

Figure 3.4 shows the circumferential strain, $\varepsilon_{\theta\theta}$, as a function of angular position at a normal force of 1 N and shear force ranging from 0 to 1 N. When there is only a normal force, the circumferential strain is nonzero only at the point of contact ($\theta = 90$) due to the Poisson's effect. When a shear force is applied, relatively constant tensile and compressive strains develop on the tail- ($\theta < 90°$) and head-side ($\theta > 90°$) on the respective sides of the shear force vector. The circumferential strain is near zero on the compressive side $\theta > 90$. Circumferential strain in the tensile region ($\theta < 90°$) is a strong function of shear force yet a weak function of angular position (<4%). According to the classical belt friction problem, the circumferential strain should decrease from the point of contact to the proximity of the fixed boundary due to friction; however, with the static friction coefficient of 0.04, there is no significant variation with position. This suggests that the sensors could be positioned anywhere along the sensor skin, without sacrificing sensitivity, as long as they are sufficiently far from the point of contact with physical objects where they might be influenced by Poisson's effect. Placing the sensors near the nail bed reduces the probability of the sensors being subjected to interference from normal forces and makes room for other sensor modalities, such as normal force or temperature, that might benefit from close proximity to the point of contact.

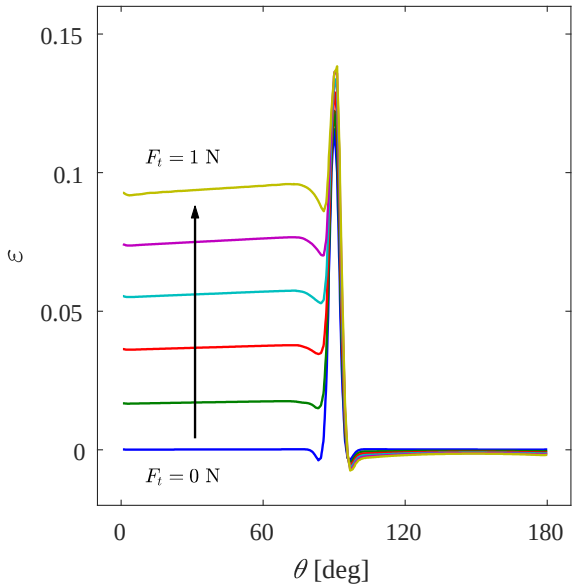

Figure 3.4 Circumferential strain at the midline of skin thickness with respect to angular position with a normal force of 1 N. The origin of the angular position is (0,0) in Figure 2.1, where θ = 90 ° is the location where the external force is applied. In this example, the compressive side is where θ > 90 ° and the tensile side is θ < 90 °. The applied tangential force magnitude increases from F_t=0 (bottom blue line) to F_t =1 N with 0.1 N increments along the direction of the arrow. Circumferential strain in the tensile region (θ < 90 °) is a strong function of shear force yet a weak function of angular position. The circumferential strain is near zero on the compressive side θ > 90. At the point of contact, θ = 90, the strain is a function of both normal and shear force due to Poission's effect.

The shear sensor skin sensitivity can be estimated using a simple analytical model with a few assumptions to validate the numerical simulation results. Considering the skin with uniform cross section, negligible friction with underlying finger core, uniform strain distribution across z direction as indicated in Figure 2.1, the circumferential strain at the location of the strain gauge can be simply represented as F_t/EA, where F_t is the applied shear force at the fingerpad, E is

Young's modulus of the PDMS, A is the cross section area. The normalized sensor response is $(F_t \cdot F)/(EA)$ where F is the gauge factor. The sensitivity is then $F/(EA) = 0.088\ \mathrm{N}^{-1}$.

Figure 3.5 shows the predicted normalized sensor response, $\widetilde{\Delta R}$, as a function of the applied shear force for 1 N of normal force. The simulations show that the sensor response is linear with applied shear force over most of the small shear forces examined here. The inset of

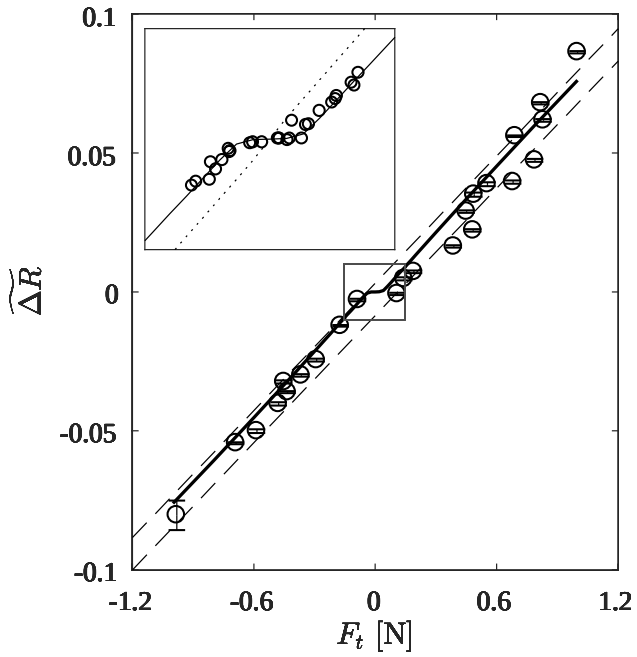

Figure 3.5 Experimental (circles) and computational (solid line) normalized resistance sensor response as a function of the applied shear force. The applied normal force is 1N and the range of the shear force is ± 1 N. The dashed grey lines show the experimental data prediction interval at a 95% confidence level. The 95% confidence interval of each data point is presented using error bars, but is too small to discern because it is smaller than the marker. The inset shows a magnified view of the experimental and computational normalized resistance sensor response with respect to shear force in the range of ± 0.15 N. The grey dotted line shows the simulated prediction of a zero-friction device. It can be inferred that the sensor performance for small shear forces could be improved by reducing the friction between the shear sensor skin and the fingertip.

Figure 3.5 shows the predicted normalized sensor response as a function of the applied shear force over a smaller range of shear forces (<0.15 N) to elucidate the sensor deadband due to the friction between the sensor skin and the rigid core. The sensor response remains at zero before the shear force overcomes the static friction force and the skin is free to slip against the rigid core, thus the deadband region increases with the normal force. At moderate normal forces of 1 N and friction coefficient as 0.04, we predict the minimum shear force measurement to be the product of two quantities as 0.04 N and similar threshold of 0.05 N is determined from experiments. The simulation is further compared with simple analytical predictions in Figure 3.6, showing good agreement of the deadband prediction as well as the sensitivity at high shear forces.

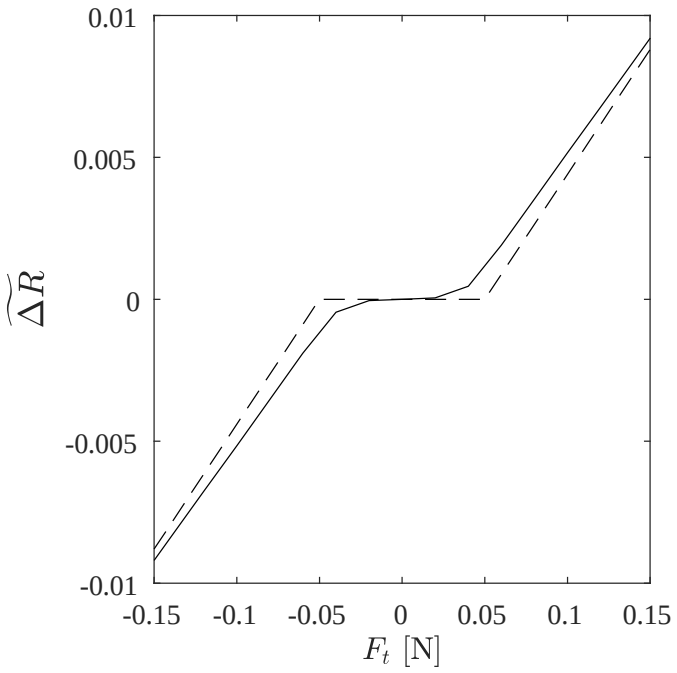

Figure 3.6 Computational (solid line) and analytical estimated (dashed line) normalized sensor response as a function of shear force. Simple analytical calculation predicted similar deadband as the numerical model, with matching sensor response at higher shear force as well.

Table 3.1 Sensitivity of the shear force sensor as calculated from computational models and experimental characterizations under different normal forces. Experimental sensitivity calculated from linear regression of shear force magnitude under 1.2 N.

Normal force [N]	**Sensitivity [N^{-1}]**	
	Computation	Experiment
0.5	0.078	0.078
1.0	0.078	0.076
1.5	0.078	0.080
2.0	0.078	0.080
Average	0.078	0.078

The slope of normalized sensor response with respect to the applied shear force throughout the working range is defined as the sensitivity. Table 3.1 shows that the predicted sensitivity for several applied normal forces ranging from 0.5 N to 2 N is 7.8 %/N. The predicted sensitivity does not change with the applied normal force, suggesting that the response of the shear sensor, in the light touch regime, is independent of the applied normal force. This is advantageous because the shear force can be resolved without knowledge of the normal force.

4. Fabrication Methodology

In this study, conventional soft lithography fabrication techniques were used to create 50 μm microchannels in PDMS. We fabricated the resistive microfluidic sensor using soft lithography and here we provide specific technical details relevant to our sensor fabrication [65]. The master for the serpentine channel was fabricated by first spin coating (PWM32, Headway Research, Garland, TX) SU-8 2025 photoresist (Microchem, Westborough, MA) at 1500 rpm onto a 4 in. silicon wafer. The wafer was soft baked by ramping up to 95 ℃ at 120 ℃/hr for 7 mins and cooling to room temperature at 240 ℃/hr. The master was exposed for 60s in a broad wavelength aligner (AB-M, ABM, Scotts Valley, CA) whose intensity is 8.88 mW/cm^2 at 365 nm. Then the wafer was post baked by ramping to 95 ℃ at 300 ℃/hr, for 7 mins and then cooled to room temperature at 300 ℃/hr. The master was then developed for 6 mins and hard baked at 150 ℃ to improve mechanical stability. Trichloro(1H,1H,2H,2H-perfluorooctyl)silane (Sigma-Aldrich, St. Louis, MO) was evaporated onto the master in a desiccator to reduce the adhesion between PDMS and the mold. The thickness of the pattern on the master was measured to be 50 μm by a stylus profilometer (Alpha Step 200, KLA-Tencor, Milpitas, CA).

We used PDMS with a 10:1 elastomer to curing agent ratio (RTV 615, Momentive, Waterford, NY). Each half of the PDMS layer was fabricated using a two-step spin coating process by first spin coating at 500 rpm for 60 s, curing at 80 ℃ for 1 hour in a desiccator under vacuum, and repeating to get a 0.3 mm thick layer. The patterned layer was peeled from the wafer and cut into desired shape of 47 mm by 20 mm with serpentine strain gauges that have a total sensor area of 7 mm by 3 mm. Reservoirs for each strain gauge were created by punching the patterned layer with a 710 μm cutting edge diameter, tin coated stainless steel puncher (CR0350255N20R4, SYNEO, Angleton, TX, USA). We bonded the patterned PDMS film to a

0.3 mm thick flat piece of PDMS, fabricated by spin coating PDMS on a blank wafer, using 30s of oxygen plasma treatment (PDC-001, Harrick Plasma, Ithaca, NY, USA) with a 500~600 mTorr pressure and RF power of 30 W. The patterned PDMS film was brought into contact with the flat PDMS film immediately after treatment and visual inspection for air entrapment. The assembly was elevated to 80 ℃ for 1 hour to increase the bonding strength. For the integrated sensor, we placed a 100 g weight to apply uniform pressure across the sensor area in order to promote bonding strength. We injected eGaIn (Gallium Indium Tin Eutectic, GalliumSource, LLC, Scotts Valley, CA, USA) into each strain gauge with a 22 gauge blunt needle (Weller KDS2212P, Apex Tool Group, Sparks, MD, USA). Two hundred fifty micron diameter copper wires (42978, Alfa Aesar, Ward Hill, MA, USA) were placed into each reservoir and sealed by dispensing uncured PDMS over the reservoirs and copper wires. The assembly was brought to 80 ℃ for 1 hr in an oven to cure the PDMS that seals the reservoirs and adheres the copper wires to the PDMS film. Figure 4.1 shows the fully assembled artificial skin embedded with eGaIn-filled microchannel strain gauges.

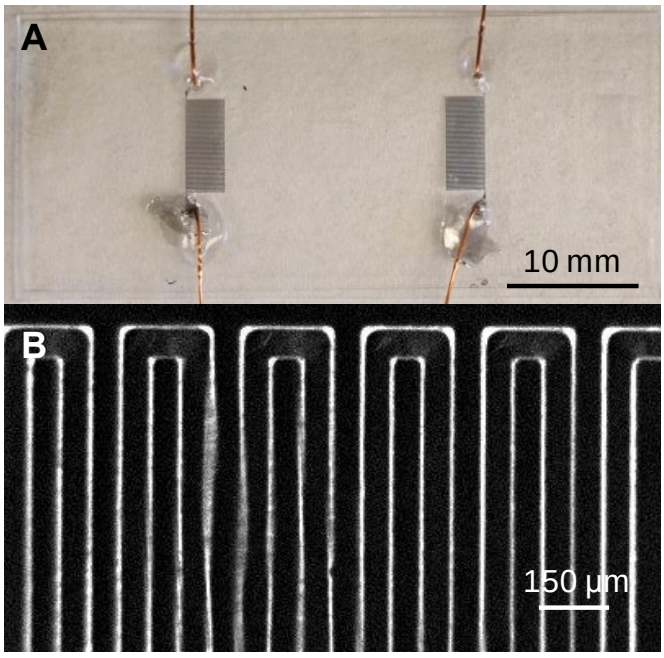

Figure 4.1 Resistive liquid metal strain gauge embedded in artificial skin: (A) an assembled device shows the eGaIn microfluidic channels embedded in PDMS. (B) microscopic view of the microchannel adjacent to a reservoir.

5. Benchtop Characterization

In this chapter we present static calibration of the shear sensor skin as well as dynamic characterization under stepwise unloading, incipient slip and controlled vibration.

5.1 Static Characterization

We mounted the shear sensor on a three-dimensional linear stage to evaluate its performance under controlled normal and shear force loading, as shown in Figure 5.1A. Three manual linear stages (433, Newport, Irvine, CA, USA) were assembled with right angle brackets (AP90, Thorlabs Inc., Newton, NJ, USA) to form three translational degrees of freedom, and were then fixed to an optical breadboard (PBH11105, Thorlabs Inc., Newton, NJ, USA). The stages were actuated manually with adjustment screws and Vernier micrometers (AJS100-2, SM-50, Newport, Irvine, CA, USA). A rotational stage (481-A, Newport, Irvine, CA, USA) was incorporated to enable fine-tuning of the direction of force loads and ensure that shear force loads were parallel to the fingertip surface tangent. Two acrylic plates were used to fasten the artificial skin to the radial and ulnar aspects of an artificial fingertip that was fabricated from an acrylic half-round with length of 20 mm and diameter of 12 mm. The fingertip was rigidly attached to the stage. The copper wires originating from the sensor reservoirs were soldered to 8 mm by 8 mm copper pads that were placed beside the plastic fingertip, adjacent to the sensor reservoirs. The copper pads provide stress relief for attachment to the external electronic equipment.

The interface between the PDMS film and acrylic half-round was lubricated by gear oil (SHC 627, Mobil, Irving, TX, USA). A force/torque (F/T) transducer (Nano 17, ATI, Apex, NC) was mounted above the sensor to provide an independent measure of the forces applied to the

sensor skin. The force transducer was attached to a loading tip that consisted of a 14 mm diameter cylindrical acrylic plate. The stage supporting the sensor skin was manually actuated to displace the sensorized fingertip relative to the force loading tip. Normal and shear force profiles were simultaneously measured by the sensor skin and force transducer.

Figure 5.1B shows the external electrical equipment. The two sensor strain gauges were connected in series with a sourcemeter (6430, Keithley, Cleveland, OH, USA) applying 5mA DC current. According to a simple convection analysis, Joule heating should not result in an increase of temperature of more than 5 ℃. We measured the voltages across each strain gauge using a low frequency data acquisition card (Personal Daq/55, Measurement Computing, Norton, MA) at 10 Hz for static characterization or a high frequency data acquisition card (DT9826, Data Translation, Marlboro, MA) for dynamic tests of stepwise unloading and vibration. Customized LabView (National Instruments, Austin, TX, USA) program collects the voltages and displays the sensor resistance response.

Figure 5.2 shows the circuit diagram of the data acquisition system used to collect the strain gauges' response. The two strain gauges in the shear sensor skin are connected in series and a constant current is applied from a current source. The voltages across each strain gauge are measured by a DAQ device using differential input. Wires from gauge 1 are fed to the corresponding high end (1H) and low end (1L) of the first DAQ channel, and those from gauge 2 to the second channel (2H and 2L). The strain gauge resistances are calculated using the measured voltages and the known current using Ohm's Law.

In the static characterization experiments, we applied normal force by moving the stage vertically and then stepwise increased shear forces (0.1 N increments) by moving the stage horizontally. Each data point was averaged over 1 second. The resistances without load were measured before each loading scenario for normalization during that loading scenario only using the equation on page 24. We also performed dynamic measurements of impulse unloading, incipient slip, and vibration.

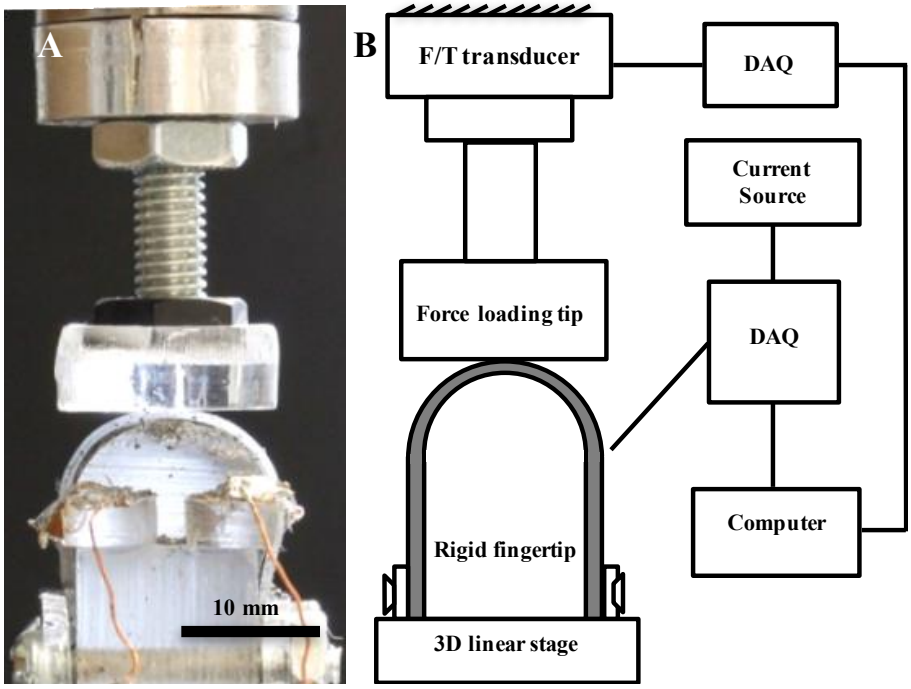

Figure 5.1 Experimental setup for sensor characterization under controlled normal and shear forces. (A) The artificial skin is mounted on an acrylic half round and the two mounting brackets are fastened by a bolt and nut. The acrylic loading tip is rigidly connected to the F/T transducer on the top. (B) Schematic of the mechanical and electrical aspects of the experimental setup. Artificial skin is shown as the grey area. The shear sensing skin is mounted on a rigid fingertip that can be displaced in 3D to generate normal and shear forces. The two sensor skin strain gauges are connected in series with a current source of 5 mA. Voltages across each strain gauge are measured by data acquisition equipment.

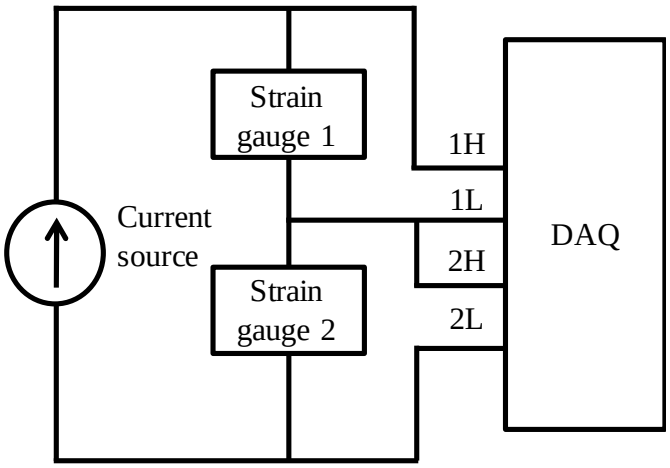

Figure 5.2 Circuit diagram of the data acquisition system. Two strain gauges in the shear sensor skin are connected in series and powered by a constant current source. The voltages across each strain gauge are measured by a DAQ device using differential input. 1H and 1L are high end and low end of the first channel, 2H and 2L are high end and low end of the second channel.

Figure 3.5 shows measurements of the normalized sensor response as a function of the shear force with a 1 N normal force. The measurements agree well with the predicted response with average deviations less than 8%. The sensor's response is repeatable with repetitive shear force up to 5 N and starts to respond at 0.04 N as predicted, with 1 N applied normal force due to static friction. The simulations show that the minimum shear force is required to overcome static friction and exhibit a linear response to applied shear force depending on the friction coefficient and applied normal force. We define the noise floor as the standard deviation of the normalized sensor response over a 1s measurement interval at a constant shear force value. Using this definition, the average noise floor is 1.6 mN, which results in a dynamic range (with a maximum of 5 N) of more than 10-bits. We subject the sensor to various normal forces with no applied shear force, which should not result in any measured shear force if the sensor is properly

decoupled, and show that the sensor reports a normalized sensor response of less than 1.24E-4 (or 1.45 mN), which is less than the noise floor. The drift of the sensor is evaluated by the standard deviation of the sensor response to a constant shear force load over time. The sensor was loaded with F_n = 0.5 N and F_t = 0.15N for 1 hr and data were collected at 0.01 Hz. The standard deviation of the normalized sensor response is 1.48E-4 (or 1.73 mN). The precision of the shear sensor skin is characterized by a prediction interval that was calculated to be $\pm$0.0802 N at 95% confidence. The prediction interval is derived from the linear regression analysis as the range in which a future measurement might fall at a certain confidence level. It reflects the confidence in the resolved shear force and the static calibration and is determined by,

$$\pm t_{\frac{\alpha}{2},n-2} S_{yx} \sqrt{1+\frac{1}{n}+\frac{(x_{n+1}-\bar{x})^2}{\sum(x_i-\bar{x})}},$$

where x and y are $\widetilde{\Delta R}$ and F_t respectively, $t_{\alpha/2,n-2}$ is the t value that corresponds to a confidence level of $(1-\alpha)$ with $n-2$ degrees of freedom, n is the number of data points, and S_{yx} is the standard error of the estimate.

Figure 3.5 shows that the data points are scattered while the error bar is much small than the marker itself. Such discrepancy between resolution and accuracy is usually referred to as hysteresis among resistive based devices. [28], [39], [73] The accuracy of the sensor describes the variation of sensor response among independent trials and reflects the confidence of the resolved shear force. It is derived from the prediction interval calculated from the linear regression analysis of the static characterization. The prediction interval is determined to be 0.04 N at confidence level of 68% and 0.08 N at 95%.

The responses of two strain gauges are presented separately as a function of shear force as the change of their resistance ΔR being either $R_1 - R_{1,0}$ or $R_2 - R_{2,0}$ with respect to resistances with zero load indicated by the subscript 0. Figure 5.3 shows a plot of change of resistance versus shear force experimentally (markers) and computationally (lines) to both positive and negative, *x*-direction shear forces (respective to Figure 2.1). When shear force is in the positive *x*-direction, the strain gauge on the tail-side of the shear force vector is in tension and presents strong linear relationship. The strain gauge on the head-side of the shear force vector is in compression and experiences negligible strain magnitude due to buckling. Such behavior is observed in both simulation and experiments. These results show that the strain sensor that is in

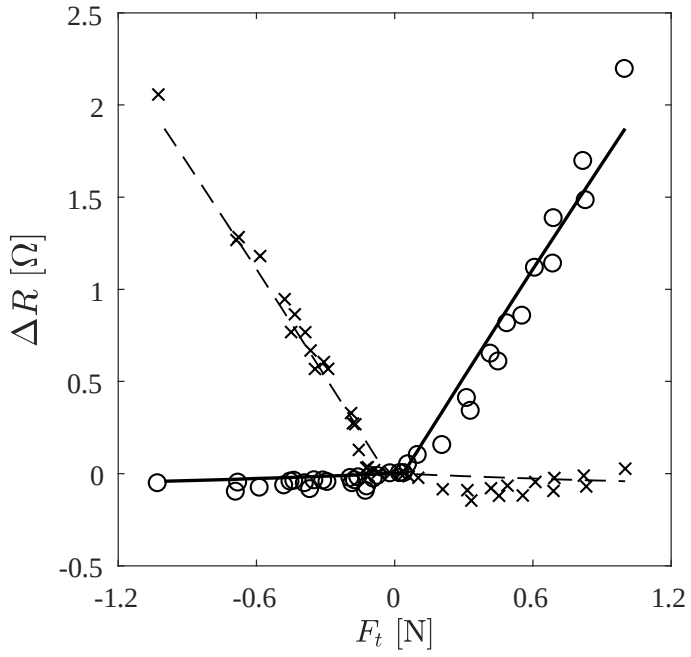

Figure 5.3. Experimental and computational resistance change of the strain gauges as a function of the applied shear force. Using Figure 2.1 as a reference, the left and right sensor responses are respectively shown as circles (experiment) and solid line (model) or crosses (experiment) and dashed line (model). The applied normal force is 1N and the range of the shear force is 1 N.

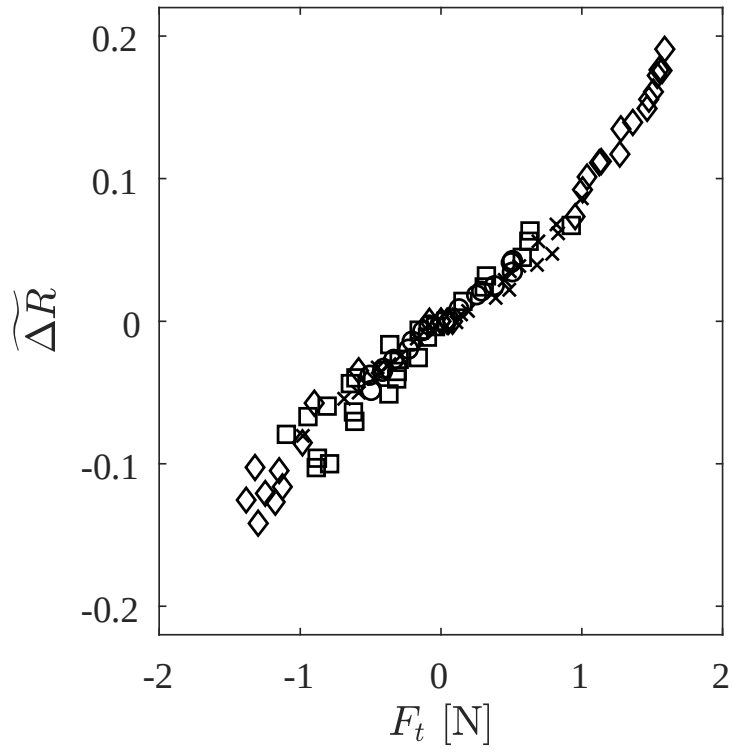

Figure 5.4 Experimental normalized sensor response as a function of shear force at normal force levels of F_n=0.5 N (Δ), F_n=1 N (□), F_n=1.5 N (○), and F_n=2 N (◊). Data points for small shear forces between -0.5 N and 0.5 N at various normal forces overlap and some are not shown to increase plot clarity. The normalized sensor response is linear at small shear force (magnitude less than 1.2 N) and exhibits increasing sensitivity at higher shear forces. The sensitivity, visualized as the slope of the data, is relatively uniform across the range of normal forces examined. The deviation from a linear calibration at larger shear forces may be the result of local high strains generated from non-uniform loading in the *z* direction (as defined in Figure 2.1).

tension generates nearly all the normalized signal response as it is defined as $\widetilde{\Delta R} = \Delta R_1/R_{1,0} - \Delta R_2/R_{2,0}$. The part of skin under compression buckles and results in negligible strain.

Figure 5.4 shows the normalized sensor response as a function of the shear force for different applied normal forces. This experiment is conducted over a larger range of shear forces ($\pm$ 1.6 N) than is shown in Figure 3.5 and exhibits a nonlinear response at higher shear forces. At shear forces greater than 1.2 N, the slope of the data increases, resulting an increase in the sensor sensitivity. Linear regression over this entire range of applied shear forces results in an error less than 30% at high shear force levels. For simplicity, we use simple linear fits to determine the sensitivity for shear force magnitude less than 1.2 N, provided in Table 3.1. These values agree well with the model predictions within 5%. If desired, a nonlinear fit can be implemented to better represent the sensor response at high shear force levels, as shown below in Figure 5.5.

We suggest that the nonlinearity observed at higher shear forces is due to the nonlinear mechanical properties of PDMS at high strain as well as the stress variation in the out-of-plane dimension (z-direction) becoming non-negligible for larger shear forces. The reduction of PDMS stiffness at high strain partially explains the increase in measured sensitivity at high shear forces. As shown in Figure 3.1, PDMS starts to soften at approximately 9% strain, and its deviation from linear elasticity can be as much as 14% at 20% strain. In addition, our two-dimensional simulation assumed a line load at the center of the fingerpad (considering a 2D simulation is infinite in the third (z) dimension), whereas in the experiments only part of the skin in the *z* direction (as defined in Figure 2.1) is loaded. Local high strain occurred in the *y* dimension that the simulation did not take into consideration.

This work is concentrated in the light touch region with small force levels; however, a more comprehensive model for a wider range of forces should likely include a 3D hyperelastic mechanical finite element model to capture the observed increase of sensitivity at high shear and

normal forces. The experimental data only shows shear force of up to 1.6 N in the light touch regime; however, the sensor is capable of measuring higher level of shear force. Unlike many capacitive sensors that saturates at some stimulation level, resistive strain gauge sensors continue to respond until mechanical failure. A simple tensile analysis yields that the PDMS artificial skin would break mechanically at 25 N of shear force. During one trial where the sensor is continuously loaded until failure, the last reported resolved shear force is 10 N.

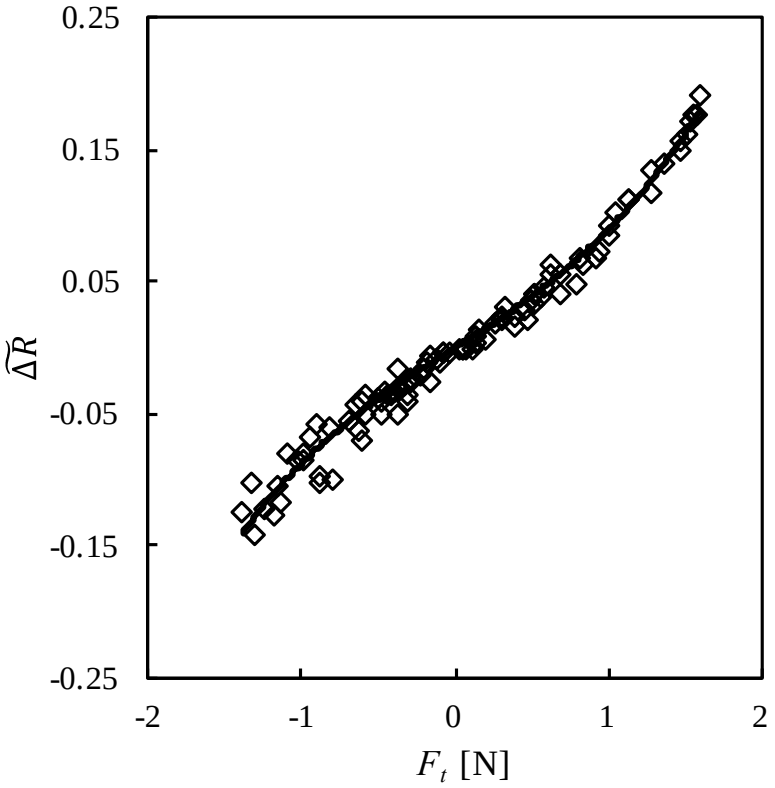

Figure 5.5 Experimental normalized sensor response as a function of shear force at normal force levels of F_n=0.5 N, 1 N, 1.5 N and 2 N. Third order polynomial fit is shown as a solid line. Data points for small shear forces between -0.5 N and 0.5 N at various normal forces overlap and some are not shown to increase plot clarity. The normalized sensor response is linear at small shear force (magnitude less than 1.2 N) and exhibits increasing sensitivity at higher shear forces.

An example of non-linear fit of the normalized sensor response with respect to shear force at normal force of 0.5 N, 1 N, 1.5 N and 2 N is presented in Figure 5.5. The solid line shows a third order polynomial fit of $\widetilde{\Delta R} = 0.0146F_t^3 + 0.0009F_t^2 + 0.0741F_t$ with a R^2 value of 0.981. Using this fit average error reduced to less than 4%.

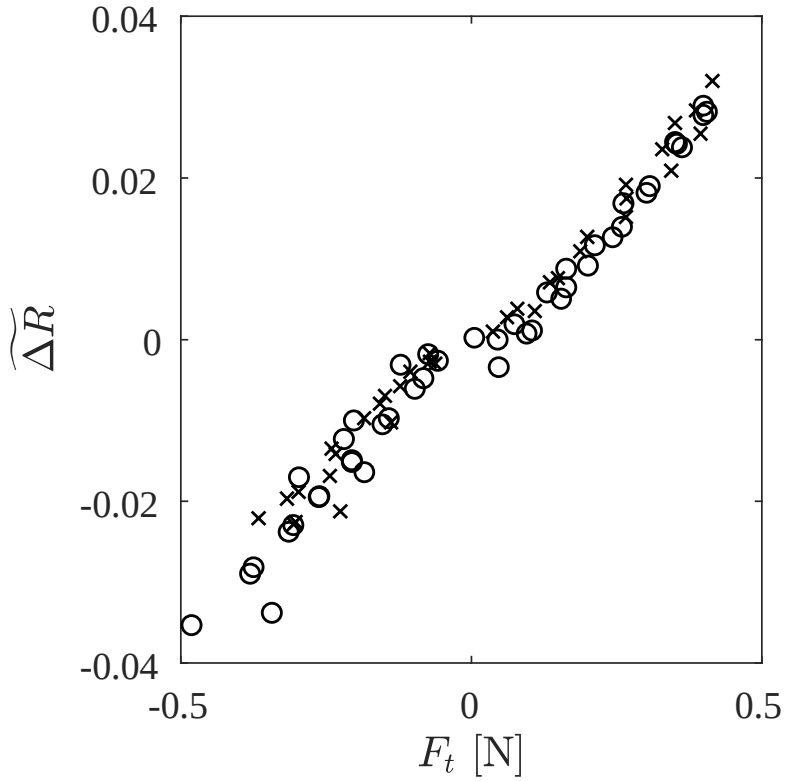

Figure 5.6 Experimental normalized sensor response as a function of shear force at F_n=1 N under room temperature (circles) and elevated temperature (crosses). Data markers overlap and change of sensitivity is not observed.

The above experiments are all performed at room temperature of around 25 ℃. In order to evaluate the sensor sensitivity variation with respect to temperature, the sensor is calibrated under F_n =1 N at elevated temperature of 40 ℃ using a heat gun. The temperature was verified by a thermocouple mounted adjacent to the shear sensor skin. Figure 5.6 shows normalized sensor response as a function of shear force at both temperatures. The sensor response overlaps

and no change of sensitivity can be observed above the data variation. Linear regression showed less than 2% of sensitivity change. The sensor response suggests that the sensitivity is likely weak function of temperature and the calibration does not change within the typical in-hand manipulation environment. The change of resistivity of eGaIn for the 15 ℃ temperature raise is approximately 1.1% [123]. The apparent strain induced by thermal expansion is governed by PDMS instead of eGaIn because relatively large reservoirs on the ends of the channels accommodate any excessive liquid metal. Linear thermal expansion coefficient of PDMS is 3.2E-4 $℃^{-1}$[124], therefore the apparent strain for the 15 ℃ temperature raise is less than 0.5%. Such variances induced by temperature changes are much less than the uncertainty observed in the experiments.

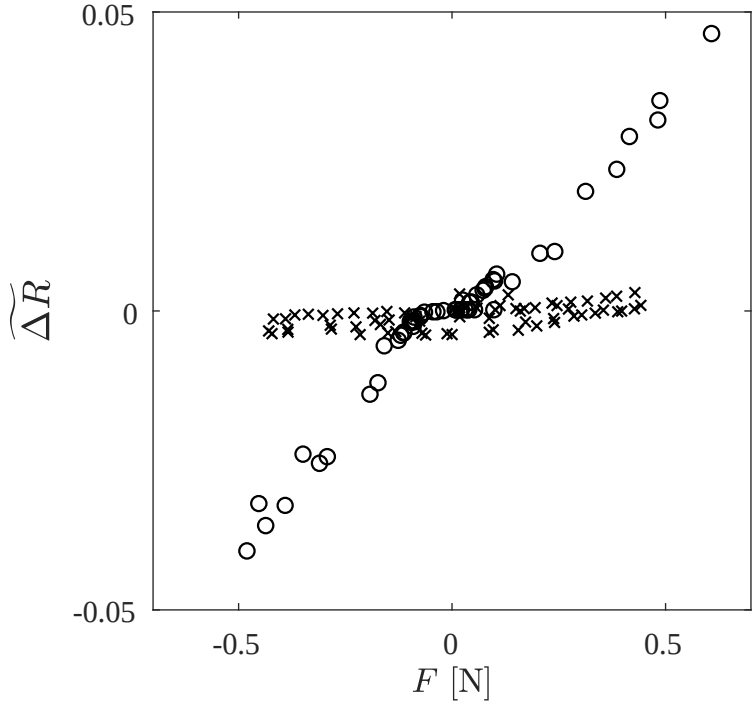

Figure 5.7. Experimental normalized sensor response to shear force in the distal/proximal direction (crosses) in comparison to the intended radioulnar direction (circles). The shear sensor skin is largely insensitive to longitudinal direction shear force.

We conduct experiments with the shear force applied in the distal/proximal direction (*z*-direction as shown in Figure 2.1) with 1N of normal force. Figure 5.7 shows experimental normalized sensor response as a function of the applied shear force. The shear sensor skin shows marginal, 0.004 N-1, sensitivity to distal/proximal shear force, which is less than 5% of its sensitivity to radioulnar direction shear force.

5.2 Dynamic Characterization

In this section, we show that our flexible microfluidic shear force sensor skin is capable of measuring dynamic shear force and vibration. We show that the sensor skin is able to resolve shear forces in benchtop experiments of stepwise unloading and slip as well as detect vibration for displacements as small as 0.43 μm and frequencies as large as 660 Hz.

Similar to section 5.1, we mounted the shear sensor on a three-dimensional linear stage to evaluate its performance under controlled normal and shear force, as shown previously for benchtop characterization experiments [94]. Two acrylic plates were used to fasten the artificial skin to the two sides of an artificial fingertip that was fabricated from an acrylic half-round with length of 20 mm and diameter of 12 mm. The fingertip was rigidly attached to the stage. The interface between the PDMS film and acrylic half-round was lubricated by gear oil (SHC 627, Mobil, Irving, TX, USA). A force/torque (F/T) transducer (Nano 17, ATI, Apex, NC) was mounted above the sensor to provide an independent measure of the forces applied to the sensor skin. The force transducer was attached to a loading tip that consists of either a steel bolt with a 4.8 mm diameter tip or a 14 mm diameter cylindrical plate with 120 grit sandpaper. The stage supporting the sensor skin was manually actuated (AJS100-2, SM-50, Newport, Irvine, CA, USA) to generate displacement and results in normal and shear force profiles which are

simultaneously measured by the sensor skin and force transducer. We measured the gauge voltages across each strain gauge using a low frequency data acquisition card (Personal Daq/55, Measurement Computing, Norton, MA) at 10 Hz for incipient slip tests and applications on robotic manipulator. We used a high frequency data acquisition card (DT9826, Data Translation, Marlboro, MA) at 52 kHz for stepwise unloading and vibration tests. The normalized sensor response was defined as, $\widetilde{\Delta R} = \Delta R_1/R_{1,0} - \Delta R_2/R_{2,0}$, where $R_{1,0}$ and $R_{2,0}$ are radial and ulnar strain gauge resistances when there is zero load, ΔR_1 and ΔR_2 are changes of resistances with respect to $R_{1,0}$ and $R_{2,0}$, respectively.

In order to assess the sensor performance with dynamic tactile events, we performed benchtop dynamic measurements of the sensor output under tactile events of impulse unloading, incipient slip, and controlled vibration. For the impulse unloading we first loaded the sensor with a given normal and shear force and then abruptly lowered the sensor away from the loading tip to generate a rapid unloading event. For the insipient slip tests, the sensor was loaded with prescribed normal force and then we increased lateral stage displacement so that the sensor slips from the load tip and finally loses contact. Figure 5.8 shows the benchtop controlled vibration test apparatus. We actuated the shear sensing skin with a piezo actuator (712A02, PCB Piezotronics Inc, Depew, NY, USA) coupled to a 10-32 stainless steel bolt as the loading tip. A laser Doppler vibrometer (OFV302, OFV2600, Polytec GmbH, Waldbronn, Germany) measured the vibration amplitude of the loading tip. The displacement and shear sensor response signal power spectrum is calculated by FFT and the power in the 2 Hz window around the actuation frequency is integrated as the signal power magnitude.

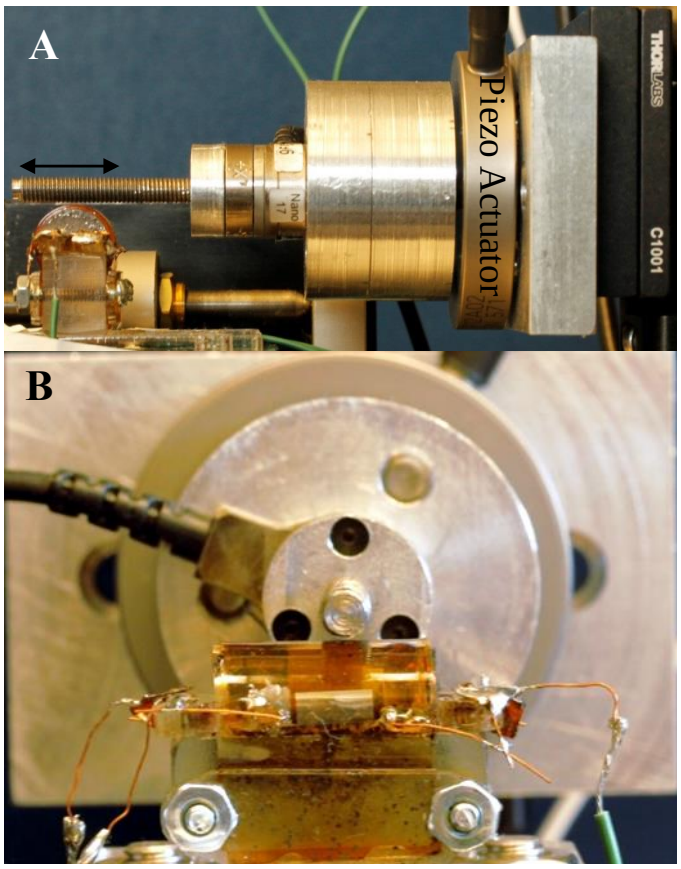

Figure 5.8 Controlled vibration experimental apparatus in two viewing angles. (A) Side view: a 10-32 bolt is used as the actuator fastened to a piezo actuator in grey. (B) Front view: the bolt is vibration in the direction in/out of the paper and the LDV laser is focused on the center of the 10-32 bolt. Such measurement is considered as reference vibration amplitude for calibration.

5.3 Stepwise Unloading

The stepwise unloading benchtop experiment is conducted by loading the sensor with normal and shear forces and then the sensing skin is suddenly withdrawn, step-wise, from contact with the loading tip. Figure 5.9 presents the normalized sensor response as a function of time during an impulse stepwise unloading event [125]. The reported shear force originates at roughly 0.15 N and drops exponentially to zero in less than 20 ms. An exponential decrease is

expected considering that the response is an overdamped dynamic system with a stepwise input. We fit an exponential curve to the response curves of three trials and find an average time scale (inferred from base of the natural logarithm) of 7.1 ms. This data suggests that the shear force sensor may be capable of capturing dynamics of up to 70 Hz, which is sufficient to temporally resolve shear force in dynamic applications such as grasp regulation or friction force monitoring.

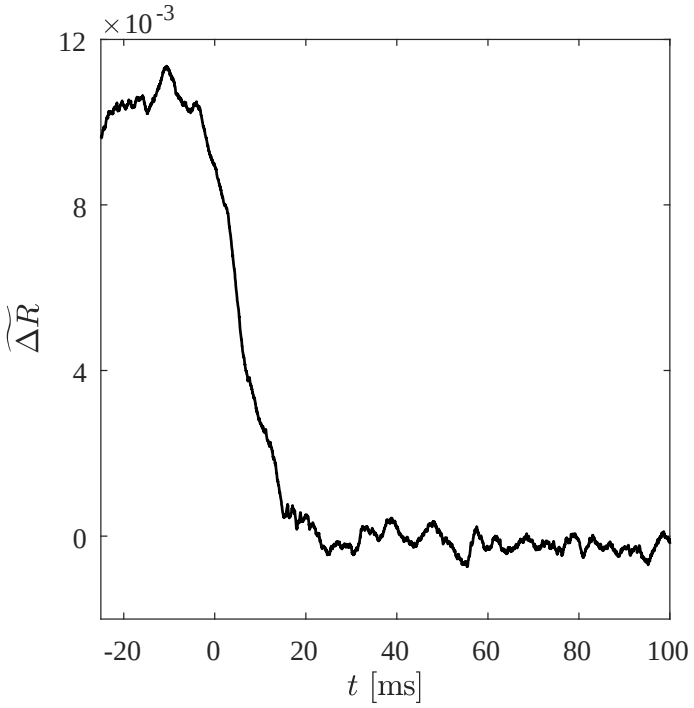

Figure 5.9 Example temporal response of the shear force sensor when stepwise unloaded. Black line shows experimental sensor response after the stepwise unloading event as it drops rapidly in the first 20 ms and finally goes to zero. Exponential model fitting is performed and a time constant of 7.1 ms is determined.

5.4 Incipient Slip Response

Figures 5.10A,B show the temporal response of the shear force sensor with lateral continuous displacement of the stainless steel and sandpaper loading tips [125]. A normal force

of 0.2 N was applied and then loading tips are translated until slip occurs and then loses contact. The resolved shear force was calculated using resistance measurement and sensitivity determined by previous static characterization experiments. As the loading tip begins to move, the measured load from both the sensing skin and the F/T transducer increase similarly until slip occurred and results in a gradual decrease in the measured shear force. The shear force continuously decreases after slip because the contact area decreases with further translation of the the circular cross section loading tip. When the loading tip is no longer in contact with the sensor, the shear force returns to zero, showing little hysteresis. Throughout the slip event the measured shear force matched with reference force measured by the F/T transducer, indicating that the shear force reported by the shear sensor skin is accurate. A useful application of a shear force tactile sensor is to detect slip and is crucial in many manipulation tasks such as grasp control. The decreasing measured shear force could be used as indicator of incipient slip and trigger actuation such as increasing torques at certain joints to re-establish the grip [45], [126]. The normal force was 0.2 N in either case, but higher maximum shear force of 0.34 N is recorded with the sandpaper loading tip compared to 0.15 N with stainless steel one. This is likely due to the greater coefficient of friction of PDMS-sandpaper relative to PDMS-stainless steel. In a controlled slip event, such as sliding along surface to examine the texture, the friction coefficient can be inferred by shear and normal force sensing. Prior knowledge of friction coefficient as well as its real-time monitoring have been shown to be essential in grasping fragile objects [45], [47], [50].

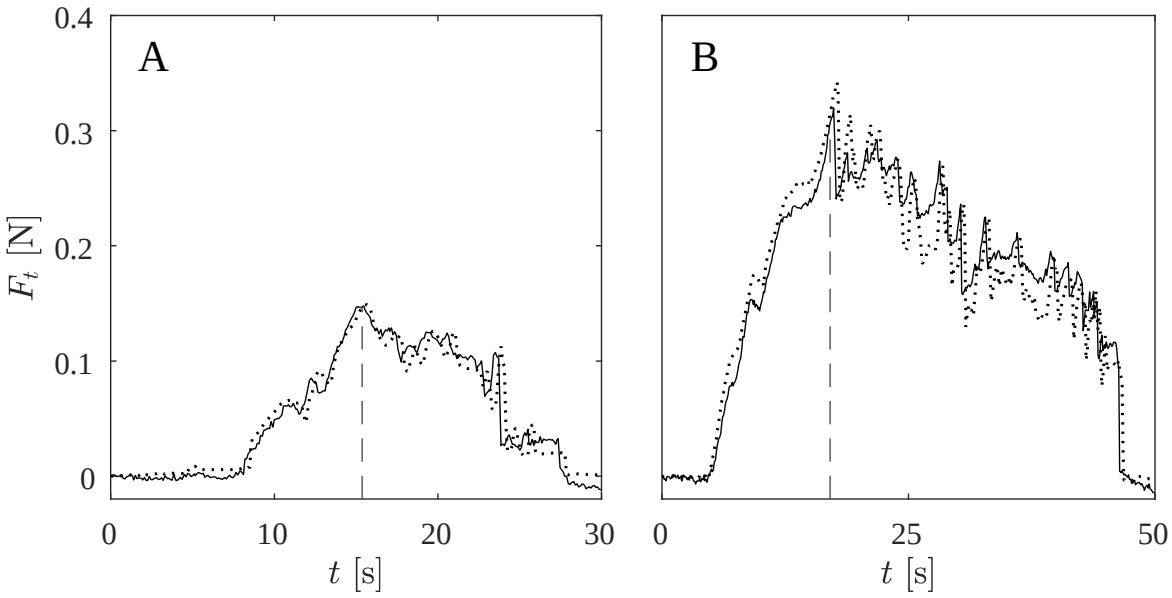

Figure 5.10 Temporal response of the shear force sensor (solid) and the F/T transducer reference measurement (dotted) during an incipient slip event using a stainless steel (A) and acrylic with sandpaper (B) loading tip. The shear force increases and then decreases when the loading tip begins to slip (denoted by a vertical dashed line). The difference between the shear force magnitudes with identical normal force on two tips indicates different coefficient of friction.

5.5 Controlled Vibration

In the controlled vibration tests, we used a piezo actuator to generate oscillating displacement. The displacement is measured by a laser Doppler vibrometer (LDV). Figure 5.11A shows the normalized shear response power magnitude and LDV vibration amplitude as a function of actuation frequencies [125]. Both the response and LDV vibration amplitude increases to the maximum as the frequency reaches the actuating system's resonance frequency at 260 Hz, then decreases as frequency continues to increase. The resonances at 105 Hz and 260 Hz diminish the ability of the experimental setup to adequately characterize sensor's

dynamic response at these frequencies. The sensor response magnitude is above the noise floor (2.4E-5) for frequencies below 800 Hz. In these experiments the maximum frequency measured

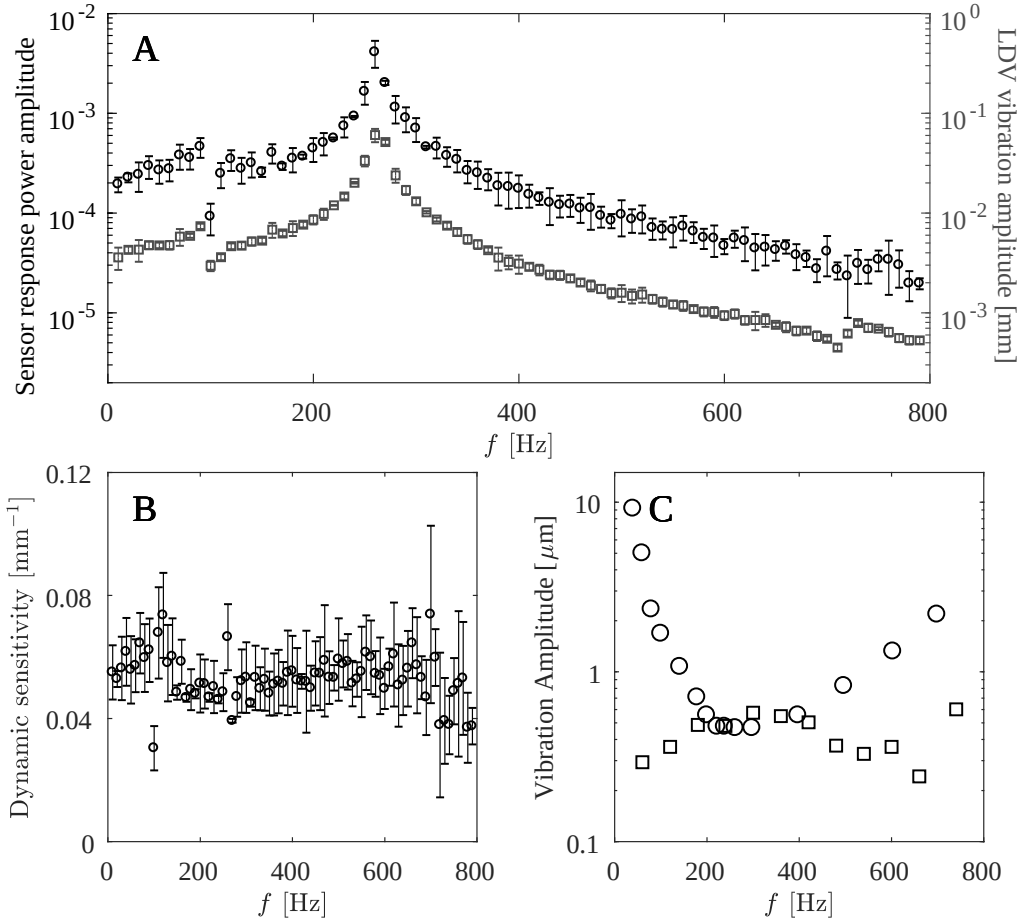

Figure 5.11 Sensor response in controlled vibration tests. (A) Shear sensing skin force signal power magnitude (circles) and actuated displacement magnitude measured by LDV (squares) at different frequencies. The sensor response closely reflects the variation of the vibration amplitude. Sensor signal is above the background noise before 800 Hz. (B) Sensor response sensitivity calculated as $(\widetilde{\Delta R}/d_{LDV})$. Data was collected in 10 Hz increment and averaged across 20 Hz. Error bars show standard deviation from 5 independent trials. The function is relatively constant throughout the spectrum within the variation of error bars.. (C) Displacement detection threshold of shear sensing skin (squares) and human (circles) as a function of frequency Human sensitivity data is extracted from Fishel and Loeb [16] . The sensor is equivalent or better than human average in over the detectable frequencies.

is limited by the piezo-actuated vibration amplitude at high frequencies.

Figure 5.11B shows sensor dynamic sensitivity as the quotient of shear sensor response magnitude and actuated displacement magnitude measured by LDV shown in Figure 5.11A. The dynamic sensitivity stays relatively constant showing that the sensor is able to faithfully measure the amplitude of a periodic displacement for a wide range of frequencies below 800 Hz, which is the limit of current piezo actuator to provide sufficient displacement amplitude at high frequencies. The peaks around 100 Hz and 260 Hz in Figure 5.11A indicate natural frequencies of the actuating system. Figure 5.12 shows actuated displacement measure by LDV with concentration at these frequencies. The actuated input clearly presents two peaks around these frequencies and is significantly higher than the rest by almost an order of magnitude. Such great input might drive the sensor skin into non-linear region and deviate from the linear assumption to calculate the dynamic sensitivity as the quotient of the sensor response amplitude and actuating vibration amplitude. Future work may shift these natural frequencies higher so that the characteristic of the actuating vibration amplitude will be constant throughout the bandwidth of interest. Preliminary results shows indication that increasing the stiffness and decreasing the mass of the actuating system would increase the natural frequency.

The limit of detection (LoD) is defined as the lowest amplitude of vibration that can be reliably detected and differentiated from zero vibration amplitude and represents the vibration detection threshold of the shear sensor skin. [127] Figure 5.13 shows sensor response signal power with respect to LDV vibration amplitude at 240 Hz. The sensor showed linear response to a variety of vibration amplitude and linear regression is performed to convert sensor response power to vibration amplitude. The limit of blank (LoB) (red line) is calculated from the sensor

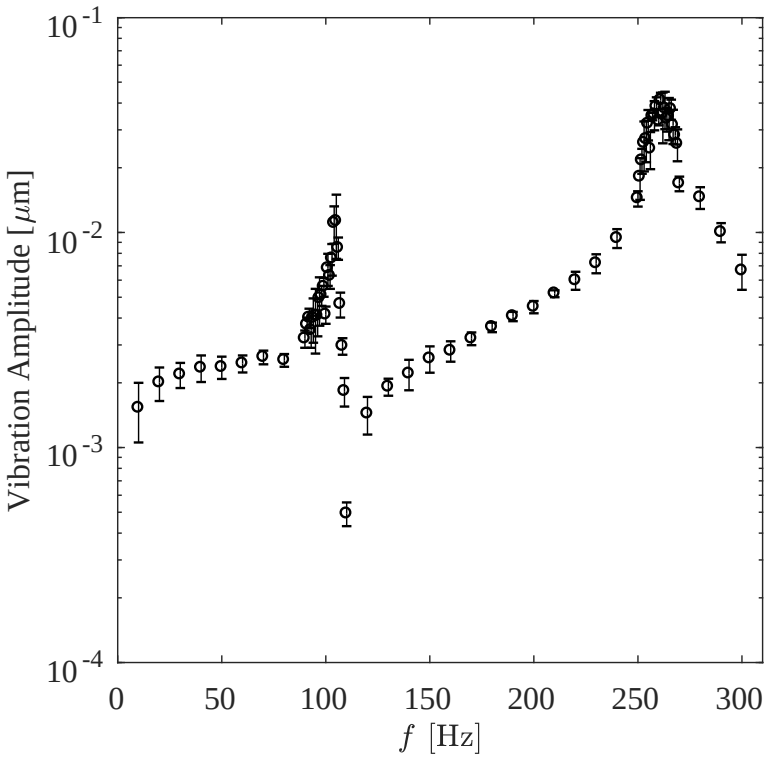

Figure 5.12 Actuated displacement magnitude measured by LDV at different frequencies with closer look around resonance. Two peaks of 105 Hz and 260 Hz can be found with amplitude significantly greater than the remaining frequencies.

response with no vibration excitation as $\mu+1.645\sigma_B$, where μ and σ_B are respectively mean and standard deviation of sensor response with no excitation. Limit of detection (LoD) (green line) is calculated from a few low amplitude trials as $LoB+1.645\ \sigma_S$, where σ_S is the standard deviation from low amplitude trials. The LoDs are calculated from all frequencies of interest and presented in Figure 5.11C.

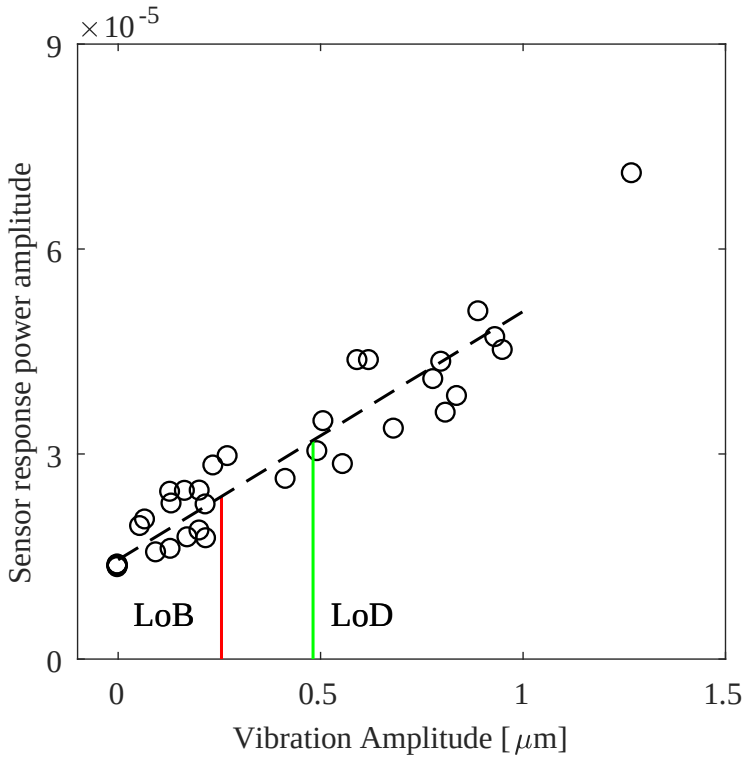

Figure 5.13 Sensor response signal power with respect to vibration amplitude at 240 Hz. The sensor showed linear response to a variety of vibration amplitude. The limit of blank (LoB) (red line) is calculated from the sensor response with no vibration excitation. Limit of detection (LoD) (green line) is calculated from the standard error of the linear fit from a few low amplitude trials.

Shear sensor skin vibration detection threshold is determined for all frequencies of interest and presented in Figure 5.11C and compared to human vibration sensitivity from Fishel and Loeb [16]. Figure 5.11C shows that a human's ability to perceive vibration decreases from 10 microns at low frequency to a minimum of 0.47 microns at 260 Hz where it increases linearly, but remains under a few microns at 700 Hz [16]. The maximum frequency vibration that a human can tactilely sense is roughly 800~1000 Hz [6], [39]. The shear sensing skin's detection threshold is relatively constant in the range of 0.3-0.6 microns across from 0-800 Hz. The shear

sensing skin outperforms human within 0-140 Hz and 500-800 Hz, and roughly equivalent to the average human between 140 and 500 Hz. Overall, the shear sensor is on equivalent or better than to human vibration sensing capabilities below 800 Hz.

6. Field Tests on Robotic Manipulator

We demonstrate the shear force sensor potential of providing critical tactile event cues in robotic applications and its robustness in more realistic operating conditions using a robotic manipulator and object manipulation experiments. In real applications, the sensor needs to be robust to electromagnetic interferences generated by robotic manipulator. The shear sensing skin robustly reported tactile events while the robotic arm performed several manipulation tasks including pick and place, drop, and handoff. Figure 6.1 shows the sensor mounted on an artificial fingertip that is attached to a BarrettHand robotic manipulator (WAM, Barrett Technology, Newton, MA). We performed pick and place, drop and handoff object manipulation experiments on a box (15.8 × 10.5 × 9.8 cm, 204 g) to examine the sensor response to various grasp and slip conditions [125]. All three tests began with the robotic manipulator grasping the box with a three-finger grip. The sensorized finger was on one side and the other two fingers on the opposite side. For the pick and place test, the manipulator lifted the box vertically 2.5 cm (over the 8 seconds), returned the box to 2 mm below its original position (at the same rate), and then released the fingers. For the drop test, the manipulator lifted the box vertically and then slowly opened its grasp until the box fell. For the handoff test, the manipulator lifted the box while a human operator applied forces to the box in the vertical direction. The manipulator was then signaled to release the grip on the box.

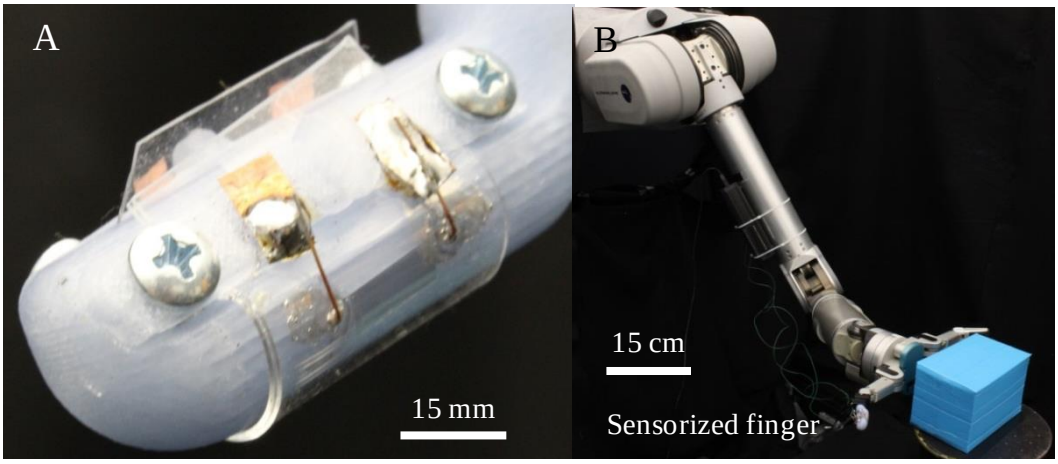

Figure 6.1 (A) Shear force sensing skin mounted on a fingertip with a radius of curvature is 6.35 mm. Mounting brackets are used to fasten the skin to the fingertip. The electrical connections to DAQ are not shown. (B) Experimental setup consisting of the robotic manipulator with one sensorized finger and two standard fingers as well as the manipulated blue box. The shear force measured by the sensor skin is in vertical direction.

Figure 6.2 shows the snapshots of different manipulation stage and sensor response to the pick and place test. The measured shear force response is zero before finger made contact with the object, then increases to a constant value around 1 N when the effector grasps and lifts the box. The shear sensor accurately measured half of the box's total weight of 2 kg m/s^2. Note the initial overshoot in the shear force due to the acceleration of lifting the box. The sensor response is constant throughout the duration of grasp until the manipulator returned the box to the operating platform by pushing slightly into the platform. Pushing the box into the platform is captured by the shear force sensor as a negative shear force (III) before it returned to around zero when the manipulator released the box. .

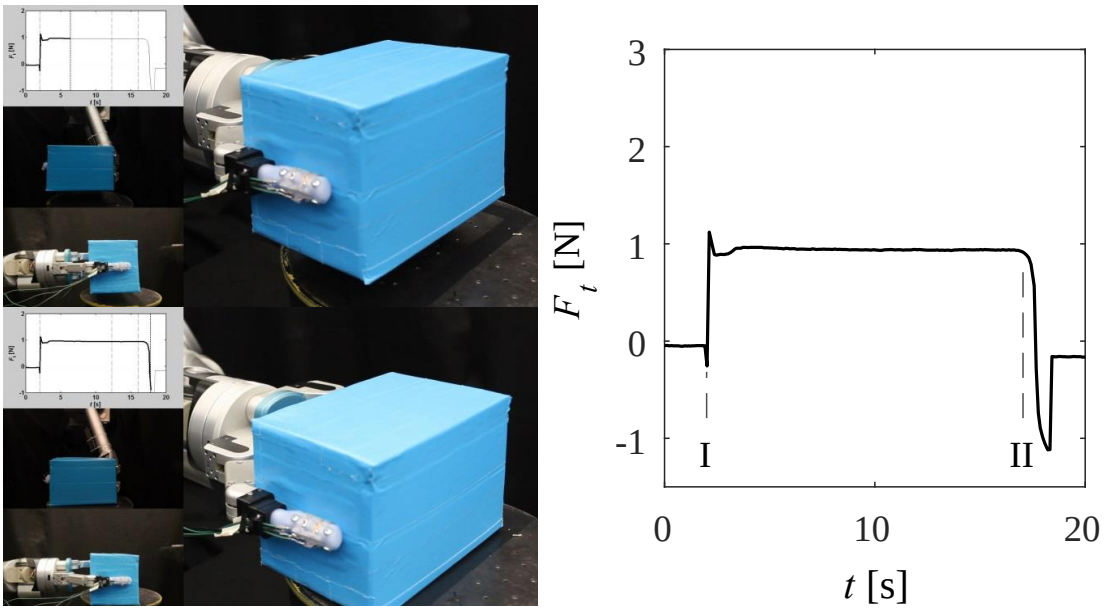

Figure 6.2 Shear force sensor response for robotic manipulation during pick and place test. Vertical lines mark events: (I) object picked up, (II) object is replaced and released.

In the pick and drop tests, shown in Figure 6.3, the shear force increases from zero to approximately 1N when the object is picked up (I). As the grasp is slowly opened, the object begins to slip and the shear force fluctuates and finally decreases to approximately zero when the object is completely released and falls away (II). The fluctuation during the release first slightly decreases, due to the object's transient vertical acceleration, and then rapidly increases to approximately 1.5 N. We interpret this sharp increase to the box shifting its pose within the grasp. As the grasp is gradually opened, the object slips from the lower stock finger and twists, reforming contact with the sensorized finger and the top stock finger at a new angle as the distance between these fingers has increased. In this new configuration, the symmetry of the force distribution is broken because the box is tilted and the lower stock finger is no longer in contact with the object and applies no force.

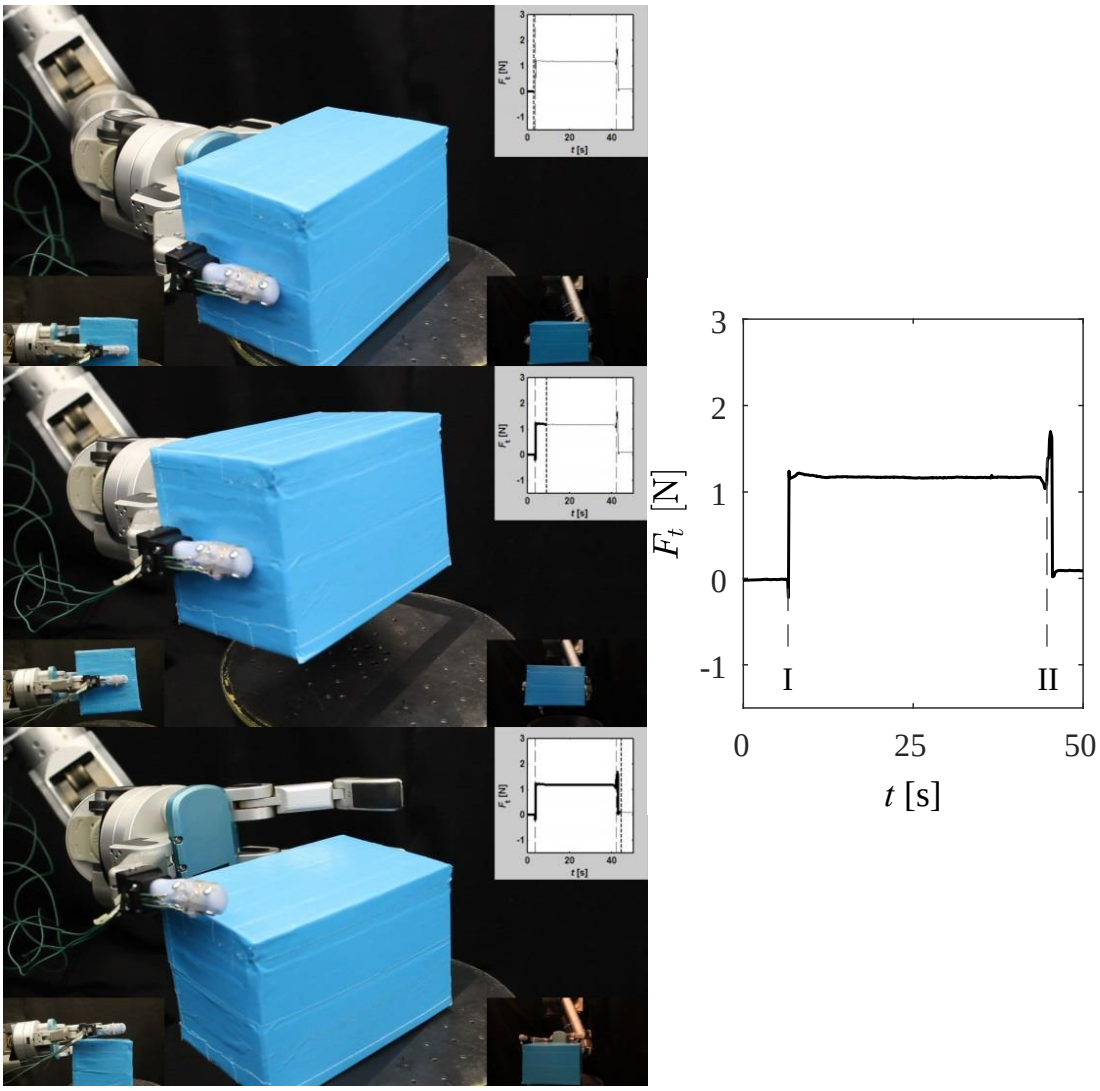

Figure 6.3 Shear force sensor response for robotic manipulation during pick and drop test. Vertical lines mark events: (I) object picked up, (II) release and drop.

Figure 6.4A shows the free body diagram of the manipulating box when it's in contact with three fingers during lift. Figure 6.4B shows the manipulating box tilted and is in contact with only two fingers, the sensorized finger at location 1 and the top stock finger at location 2. N and f represents normal force and friction force at each location, a and b are geometry measurements, m is the mass of the object. At steady state the sum of the forces are zero, so that:

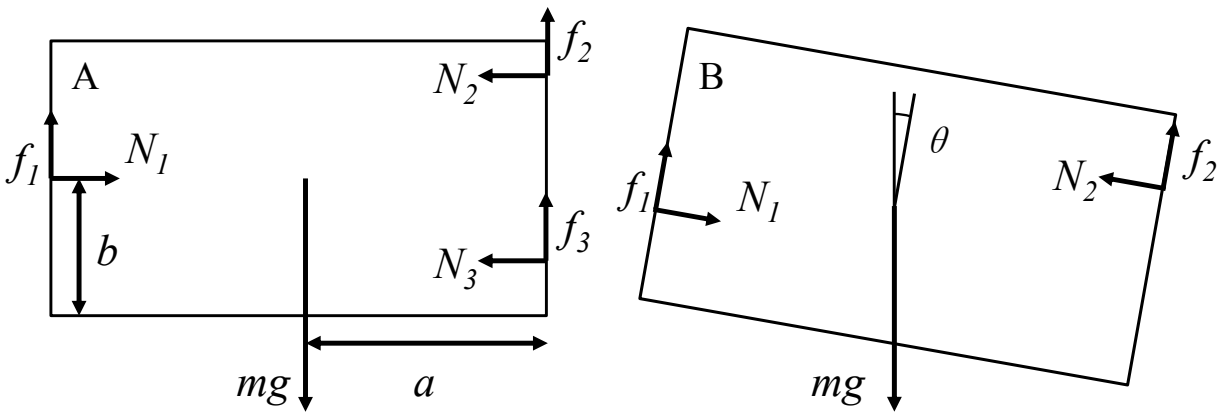

Figure 6.4 Free body diagram of the manipulating box when it's (A) in contact with three fingers during lift. Location 1, 2, 3 represents contact with three artificial fingers; (B) manipulating box is tilted and is in contact with only two fingers, the sensorized finger at location 1 and the top stock finger at location 2.

$$N_1 + mgsin\theta = N_2, \tag{1}$$

$$f_1 + f_2 = mgcos\theta, \tag{2}$$

Sum of moment is zero, so that:

$$(N_1 + N_2)b + f_2 a = f_1 a \tag{3}$$

The finger-object contact at location 2 is slipping, therefore according to Coulomb's friction law

$$f_2 = \mu_2 N_2, \tag{4}$$

1,2,4 → $$f_1 + \mu_2 N_1 = (cos\theta - \mu sin\theta)mg \tag{5}$$

1,2,3 → $$f_1 = (2N_1 + mgsin\theta)\frac{b}{a} + \mu_2(N_1 + mgsin\theta) = \left(\frac{2b}{a} + \mu_2\right)N_1 + \left(\frac{b}{a} + \mu_2\right)mgsin\theta \quad (6)$$

Plug 6 into 5 $$N_1 = \frac{mg\left(cos\theta - \left(2\mu_2 + \frac{b}{a}\right)sin\theta\right)}{\frac{2b}{a} + 2\mu_2}, \quad (7)$$

Plug 7 into 6 $$f_1 = mg\left(\frac{\left(cos\theta + \left(2\mu_2 + \frac{b}{a}\right)sin\theta\right)\left(\frac{2b}{a} + \mu_2\right)}{\frac{2b}{a} + 2\mu_2} + \left(\frac{b}{a} + \mu_2\right)sin\theta\right) \quad (8)$$

$$= \frac{mg}{2\left(\frac{b}{a} + \mu_2\right)}\left(\left(\frac{2b}{a} + \mu_2\right)cos\theta - \frac{b}{a}\mu_2 sin\theta\right)$$

When $\theta \to 0$, $f_1 \approx \frac{\frac{2b}{a} + \mu_2}{\frac{2b}{a} + 2\mu_2}mg$

The mass of the object m = 204 g. We estimate the friction coefficient to be 0.7~1.6 [128]. Therefore f_1 is estimated to be 1.28~1.47 N. Such results are in close proximity from the experimental observations of pick and drop test. The conclusion is that the measured shear force is larger than half of the object weight when stationary and estimated to be 1.3~1.5 N, which is confirmed by experimental results. As the grasp is further released, the box can no longer sustain its position by tilting and loses contact with all the fingertips, and the measured shear force rapidly decreases to near zero.

Figure 6.5 shows the snapshots of different manipulation stage and the sensor response when the robotic hand transfers the box to a human hand and then releases its grip. In these handoff tests, after the box was lifted (I), the shear force sensor reported varying shear force

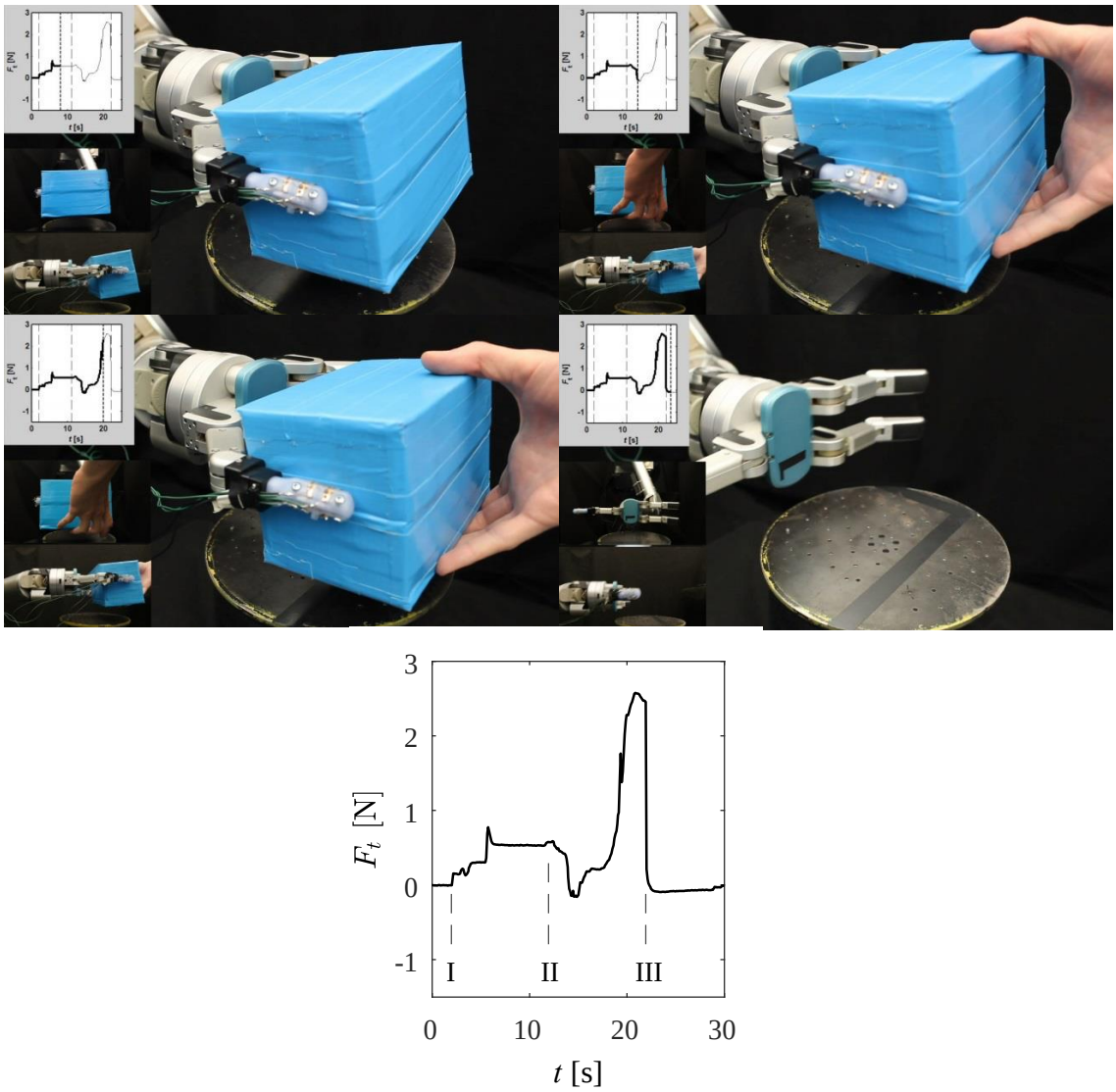

Figure 6.5 Shear force sensor response for robotic manipulation during handoff test. Vertical lines mark events: (I) object picked up, (II) start interaction with human, (III) object released.

when both the manipulator and human hand are interacting with the object (starting from II). In this case the shear force is dependent on the dynamics of the manipulating object. Depending on the direction and magnitude of the force applied by the human, the shear force that the sensor reported fluctuated. At the end of the handoff process the manipulator released the grasp on

command and shear force returned to approximately zero (III). In all three tests the measured shear force returns to approximately zero with some hysteresis that might be a result of friction and adhesion between the sensor skin and plastic fingertip surface.

The shear sensing skin's performance in the above tasks showed its ability to obtain information about shear force on the fingertip and thus finger-object interactions. The change of shear force indicates occurrence of tactile events such as grasping and slipping. Through such information, the sensor can also provide insight into human-robot interactions as shown in the handoff tests.

7. Multimodal Sensing Skin

Rich and timely tactile sensing is useful with both normal and shear sensing simultaneously forming the complete picture of the contact force vector in three spatial dimensions and dynamic vibration sensing in time domain. Spatially resolved normal force sensing, two-dimensional shear and vibration sensing can resolve contact surface and object volumetric properties such as texture, shape, weight, as well as prevent slip and regulate grasp [45]–[47], [50], [69]. In spite of such need, current tactile sensor skin solutions either concentrate on a single sensing modality, or integrate both modalities using pairs or quadruples of normal force sensors that suffer from ambiguity and reduced spatial resolution. To our knowledge, no sensor skin has demonstrated both normal and shear sensing as well as vibration on curved surfaces.

This unmet need motivates my work on a multi-modal sensor skin with distributed normal force sensors and two-dimensional shear sensing. In this section, we present a multi-modal sensing skin with 8 normal force sensing taxels and 4 shear sensing strain gauges to be mounted on a plastic fingertip. Static calibration and controlled vibration tests are performed to demonstrate the sensor skin is sensitive in the light touch regime. This sensor resolves shear force information regardless of the posture of the hand and the direction of the surface traction on the artificial skin. The normal force sensors exhibits sensitivity of 18 %/N and better-than-human performance to measure vibration. The shear force sensor showed sensitivity of 4.7 %/N in one direction and 3.2 %/N in the other.

7.1 Design and Theory of Operation

The layout of the shear force sensor enables integration with a normal force sensors located at the area of contact, e.g. a capacitive pressure sensor by Ponce Wong *et al*.[65], or a resistive spiral pressure sensor by Park *et al*. [71], [75].. The capacitive pressure sensor has issues of parasitic capacitance, poor high frequency response, and requires a ground shield to properly function. We made effort to shield capacitive sensors from electromagnetic noise using conductive polymer such as PEDOT::PSS, but found that the presence of PEDOT::PSS greatly restricted the sensor skin's flexibility, showing cracks and discontinuity when wrapped around the artificial fingertip. Spiral resistive normal force sensors tend to be more robust against electromagnetic noise and are easier to fabricate because they only consists of a single layer microfluidic architecture. We modified existing spiral normal force sensors to fit finger-sized end effectors and reduced the geometry to enhance dynamic range.

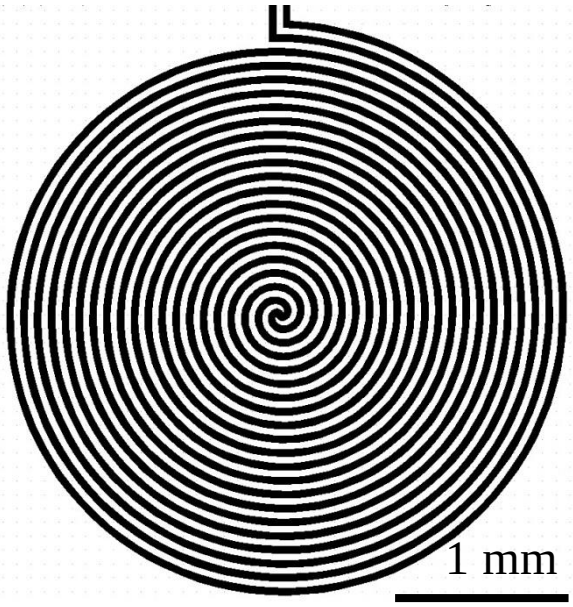

Figure 7.1 The normal force sensor pattern design. Arithmetic spiral curve is used to allow constant separating distance between the channels.

The normal force sensor pattern is shown in Figure 7.1. It consists of two arithmetic spiral curve connected at the center, with inlet and outlet on one side of the spiral. The resistance of the channel is a function of sensor total radius, channel spacing and dimension.

The expansion of previous shear sensing skin has to meet the following constraints:

1. Accommodate several normal force sensors at the location of tactile interest and 4 shear sensing strain gauges: 2 for the current lateral direction and 2 for orthogonal proximal/distal direction.
2. Can be fabricated flat on silicon wafer, cut into desired shape and conform to the curved surface of a custom-designed fingertip.
3. Provide maximum performance meeting the above constraints and fabrication limits.

We designed the sensing skin to be cross-shaped with normal force sensors in the middle and four strain gauges on the four ends, fitting a rectangular shaped finger similar to that of the BarrettHand [129]. The center pad has 2 by 2 normal sensors layout. The ulnar and radial tabs contain 1 normal sensor and 1 shear sensing strain gauge. The proximal tab contains shear sensing strain gauge only and the distal tab contains two normal force sensing taxels because there is a high interest in the normal force in this region where the fingertip interact with objects. Figure 7.3 shows the multi-modal sensing skin mounted on custom fingertip.

The sensor resistance is $R = \rho \frac{l}{A}$ with ρ as resistivity, l as total channel length, A as the cross section area. It is advantageous to maximize the normal force sensor resistance to minimize power consumption and greater measured sensor response. The channel dimension is 50 μm width and height in the goal of fabricating defect free channels that can be filled using pressure. The size of the sensor is constrained by the geometry of the fingertip. Targeted for use on a

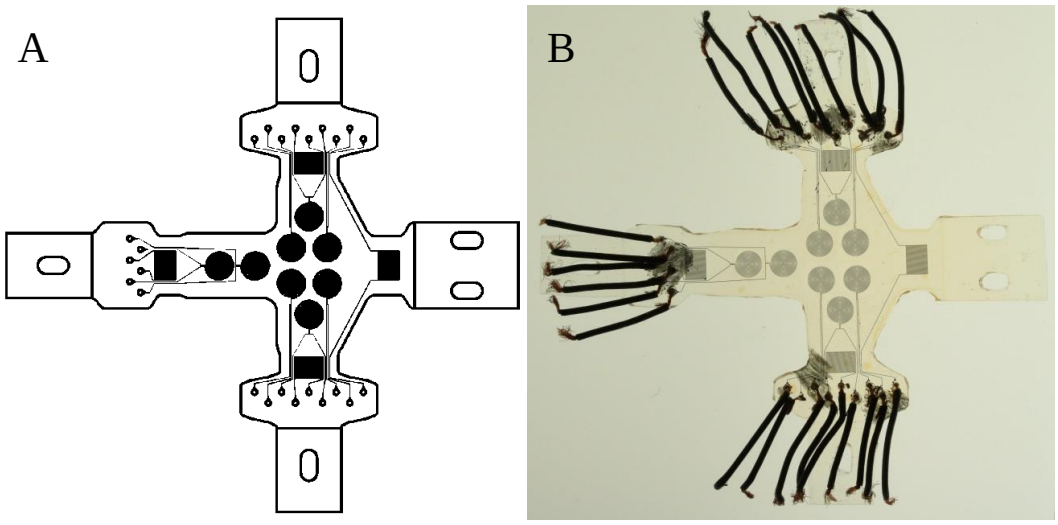

Figure 7.2 The cross shape sensor skin design (A) and implementation (B) of the skin to be conformably fitted to a fingertip with similar size of a human fingertip. Four normal force sensors are located at the center and 1 normal sensor and 1 shear sensing strain gauge are placed on ulnar and radial tabs. Proximal tab contains shear sensing strain gauge only and distal tab accommodates two normal force sensing taxels as well as shear sensing strain gauge. Sensor photograph modified to better illustrate spiral normal force sensor design.

robotic manipulator, the fingertip was custom designed with similar dimension of the BarrettHand fingertip. Then the skin was then fitted to allow conformal wrapping and sensor dimension was determined accordingly depending on the available geometry space. The diameter of the normal force sensors is 3 mm, the length and width of the shear force sensors is 3 mm and 4 mm respectively. This resulted in a normal force sensor channel that has an overall length of approximately 126 mm long and shear force sensor that is approximately 120 mm long serpentine channel made of $N = 40$ strips that are $L = 3$ mm long. The calculated nominal resistance of each strain gauge is approximately 15 Ω, which is verified in experiments.

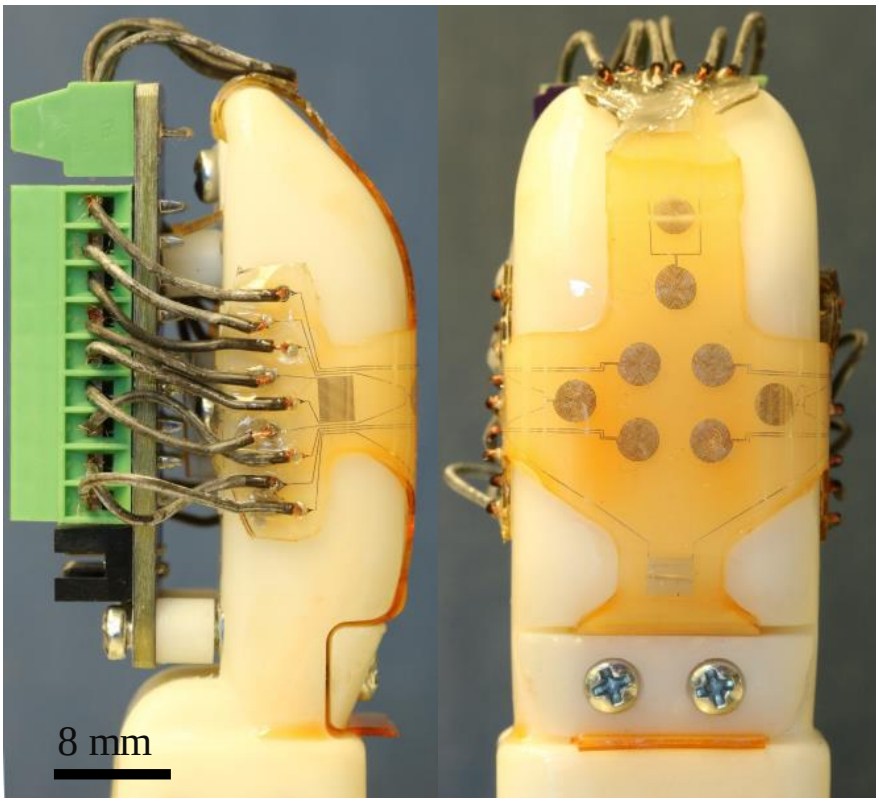

Figure 7.3 The multi-modal sensing skin picture in two viewing angles mounted on customized fingertip and connected to custom PCB. The sensing skin is fastened by mounting brackets hidden by the PCB. Flexible insulated wires are used to connect channel reservoirs to terminal blocks on the PCB. The board connects to the data acquisition equipment with 14-conductor flexible ribbon cable via black connector.

Increasing number of taxels also resulted in larger number of lead wires. There are 12 taxels and 24 reservoirs that require lead wire connection in this design. To increase robustness of the electrical connection originating from the reservoirs, 32 gauge flexible multi-strand lead wires (AS999-32, Cooner Wire Co., Chatsworth, CA, USA) were used to connect reservoirs to external electrical equipment. Figure 7.4 shows the custom PCB located at the nail bed used to

receive electrical connections from the reservoirs, connect all resistors in serial and relay the signal to DAQ devices via multiple conductor cable. Twenty four lead wires are fed into the board via terminal blocks. The board completes serial connection of all resistive taxels and output. A 14-conductor ribbon cable with 0.64 mm pitch (300-30-14-GR-0250F, CnC Tech, LLC, Chandler, Arizona, USA.) is selected to relay sensor signal for its flexibility and compact size. DC current of 5 mA is applied to the PCB and all resistors, and the DAQ system measures the voltage difference across each of all 12 resistors. Figure 7.5 shows the PCB board schematics.

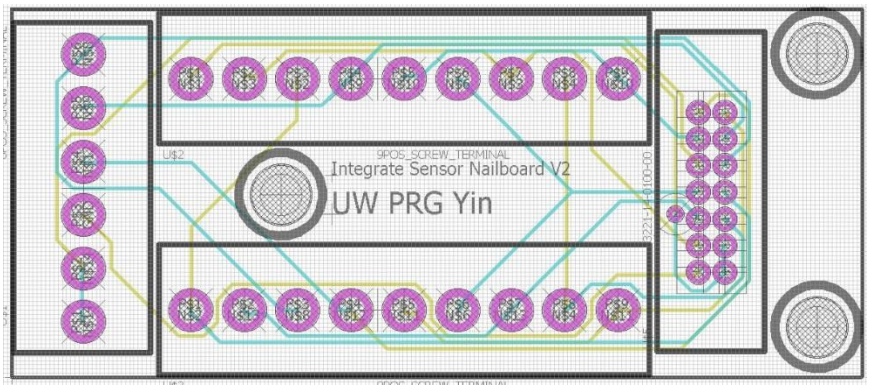

Figure 7.4 The custom PCB board used to receive microfluidic channel lead wires and relay signals to DAQ device. Three through holes for mounting are presented in grey. Figure has a drawing scale of 2.77:1.

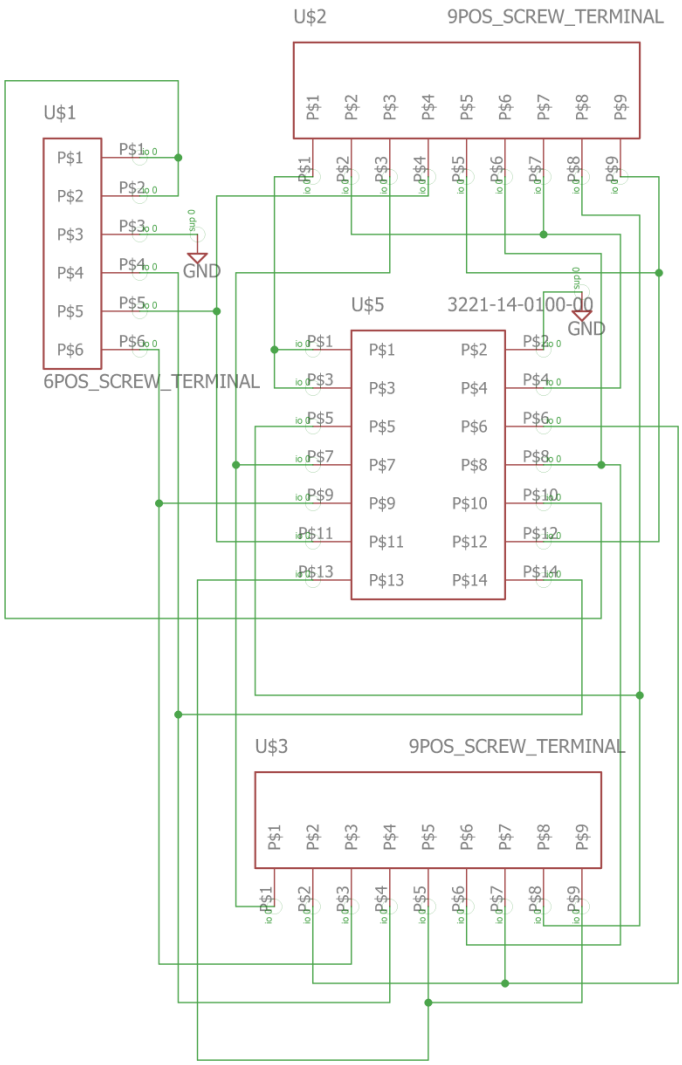

Figure 7.5 The custom PCB board schematic showing terminals and ribbon cable connector connections. Three screw terminals are connected to lead wires from microfluidic channels. The PCB connects all 12 resistors in series. DC current is applied across pin 1 and 2 in the 14-conductor ribbon cable connector which is at the highest potential end and lowest potential end of the 12 resistor series. High potential ends of 12 resistors are connected to pin 3 through 14 respectively in the ribbon cable connector.

7.2 Static Characterization

Static characterization tests were performed on the four center normal force sensors using similar procedure as section 5.1. A 10-32 bolt is used as the force loading tip to apply normal force to an individual normal force sensor. Figure 7.6 shows the experimental apparatus. During each test, normal force is loaded stepwise to 2N in increments of 0.1 N. Four normal force sensors located at the center of the fingerpad are characterized and the normalized sensor responses are calculated and plotted against measured normal force from force transducer in Figure 7.7 as different markers. Each panel represents the scenario where normal force is applied to a single sensor. Each taxel showed weak nonlinear response. Neighboring taxels showed negligible response, indicating little cross-talk and interference.

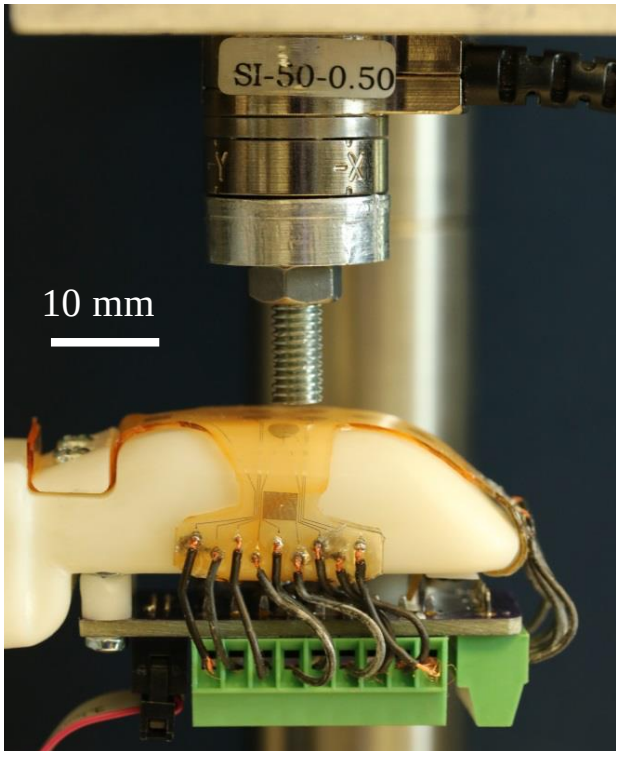

Figure 7.6 Normal force sensor calibration experimental setup. Loading tip is a 10-32 bolt and it is visually aligned to one of the normal force sensing unit during experiments.

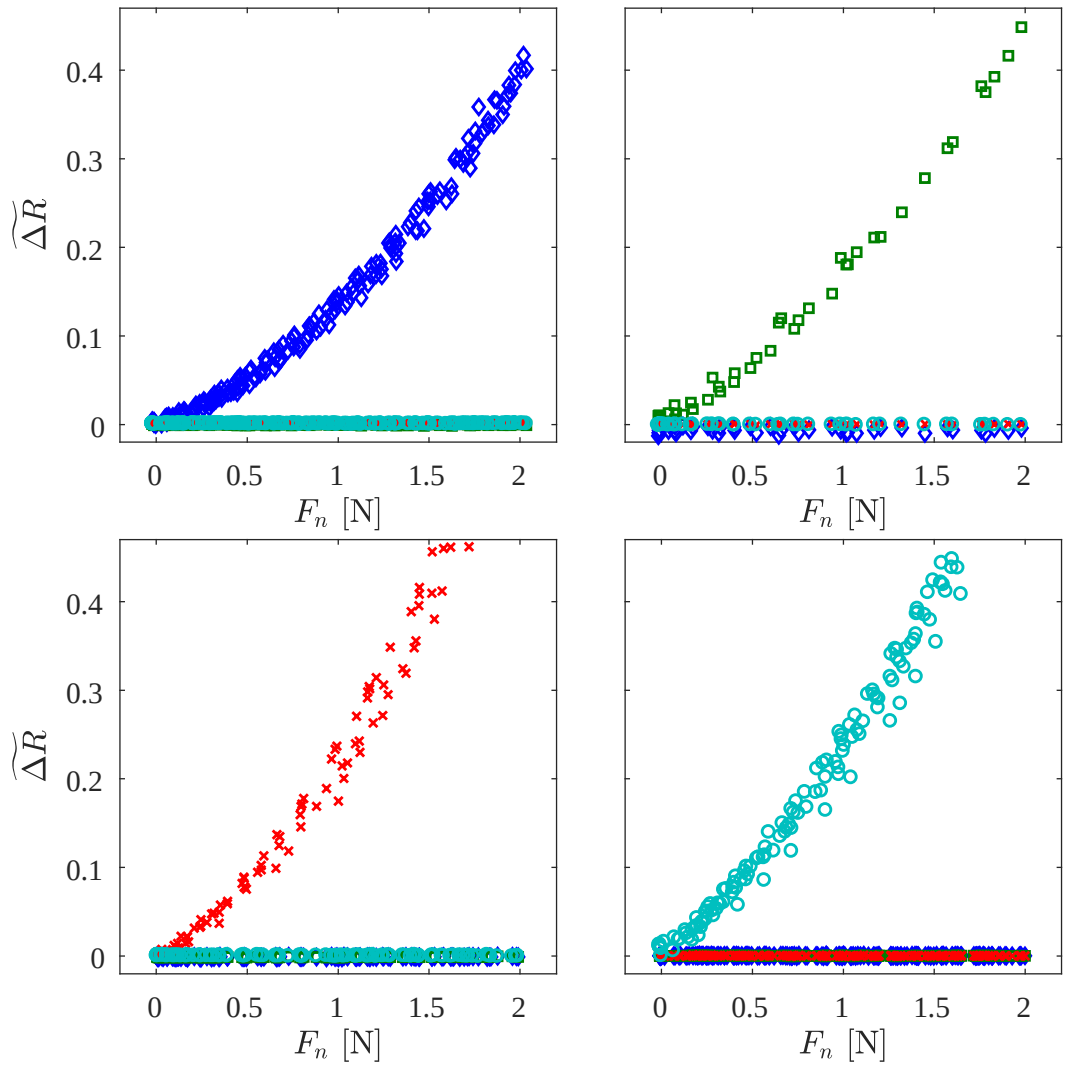

Figure 7.7 Normal force sensor calibration of four different taxels in blue, green, red and cyan respectively. Same marker in different plots represent the same taxel. In each panel a single taxel is loaded and the rest shows negligible response as desired. The loaded taxel in all scenarios showed resistance increase when subject to normal force.

Figure 7.8 shows calibration curves as normalized sensor response with respect to normal force for all four taxels. Sensitivities for the taxels are tabulated in Table 7.1. The difference in sensitivity may be the result of slight difference of geometry due to spatial non-uniformity during

fabrication or small deviations of the alignment of the loading tip. Using the standard deviation of each data point and a linear regression, the resolution is determined as 5 mN. Considering the upper limit as 5 N, the normal sensor skin can be characterized as a 10-bit.

Table 7.1 Sensitivity of the normal force sensor from linear regression of experimental characterizations where normal force magnitude is under 1 N.

Taxel number	**Sensitivity [N^{-1}]**
1	0.13
2	0.16
3	0.21
4	0.22
Average	0.18

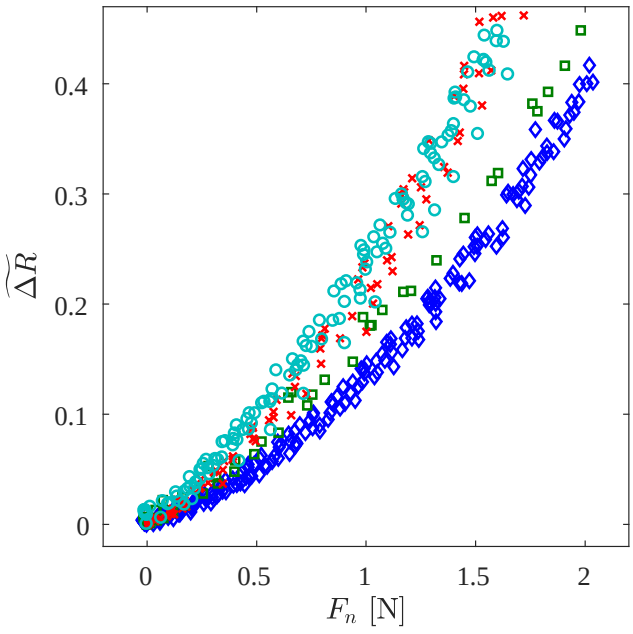

Figure 7.8 Normal force sensor calibration of four taxels when they are loaded individually. They showed similar sensitivity to normal force.

We characterize the shear force sensor response in static experiments similar to the ones for the single shear sensor. The force loading tip applies 0.5 N of normal force before it is laterally displaced while the force reading from reference transducer and shear force sensing units are recorded. Figure 7.9 shows the shear force sensor response with respect to shear force in distal/proximal and radial/ulnar direction. Both direction of shear force sensing presented monotonic response, while the radial/ulnar direction showed larger deadband. Sensitivity is characterized by the slope of the linear regression and is 4.7%/N for distal/proximal direction and 3.2%/N for radial/ulnar direction. The average sensor noise floor is 3.13E-4. Considering maximum force of 5 N the shear sensor dynamic range is around 500, or 9-bit. The difference of sensitivity and deadband between this sensor and the single dimension one might be the result of several confounding factors. First, the sharp change of surface tangent at the corners on radial/ulnar side might hinder the skin from sliding freely and applying strain to the location of the sensing taxels. The shear force sensors are located away from the center fingerpad area and located on the side of the finger where the surface radius of curvature is small (except the proximal direction gauge). They are also adjacent to the reservoirs where the skin thickness is increased due to the sealing required fixing lead wires to the reservoirs. The combined effect of locally increased thickness and small radius of curvature is that the skin cannot adhere to the surface well. In addition, there are two dimension of shear force sensing and the shear force at the fingerpad in one direction is no longer balanced by the tab in that direction alone, but also the orthogonal direction. For example shear force in radial/ulnar direction also induces shear strain in the proximal/distal tab of the skin. Therefore the strain experience by the radial/ulnar tab that is translated into sensor resistive change by the shear force sensor there is reduced.

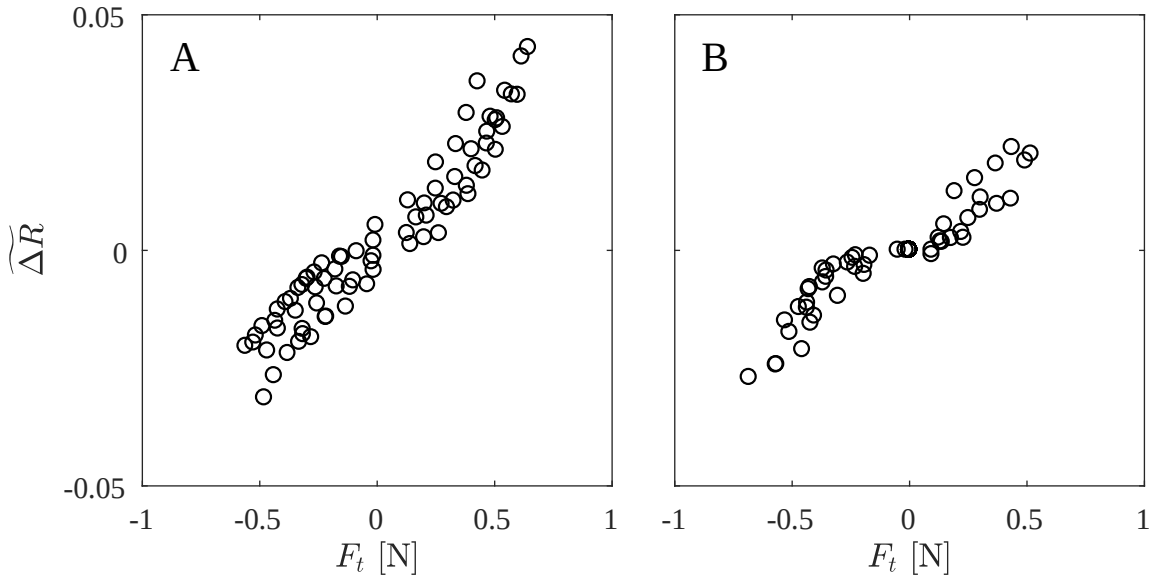

Figure 7.9 Shear force sensor calibration of (A) distal/proximal and (B) radial/ulnar direction. Sensor shows monotonic response to shear force under normal force of 0.5 N. Sensitivity shown as the slope of the calibration is higher in distal/proximal direction than radial/ulnar and the latter shows greater deadband.

7.3 Controlled Vibration

Vibration sensing using the normal force sensors is characterized similarly to section 5.3 except that the oscillating displacement is actuating the normal force sensors. The loading tip applied normal force of 0.5 N first, measured by normal force using previous calibration. Then vibration in the normal direction is actuated using the piezo actuator at different frequencies and amplitudes. Figure 7.10A shows a representative FFT plot where a single peak is found at the actuating frequency of 240 Hz. The power spectrum is integrated within 2 Hz window centered at the actuating frequency. The results are called normal force sensor response power for sensor response FFT and vibration amplitude for LDV measurement FFT. Figure 7.10B shows the normal force sensor vibration sensing calibration, which is the plot of these two variables. The

sensitivity is the slope of the calibration, describing sensor response per unit vibration amplitude. Limit of detection (LoD) is defined in the same way as section 5.3 and considered detection threshold for the normal force sensor vibration sensing.

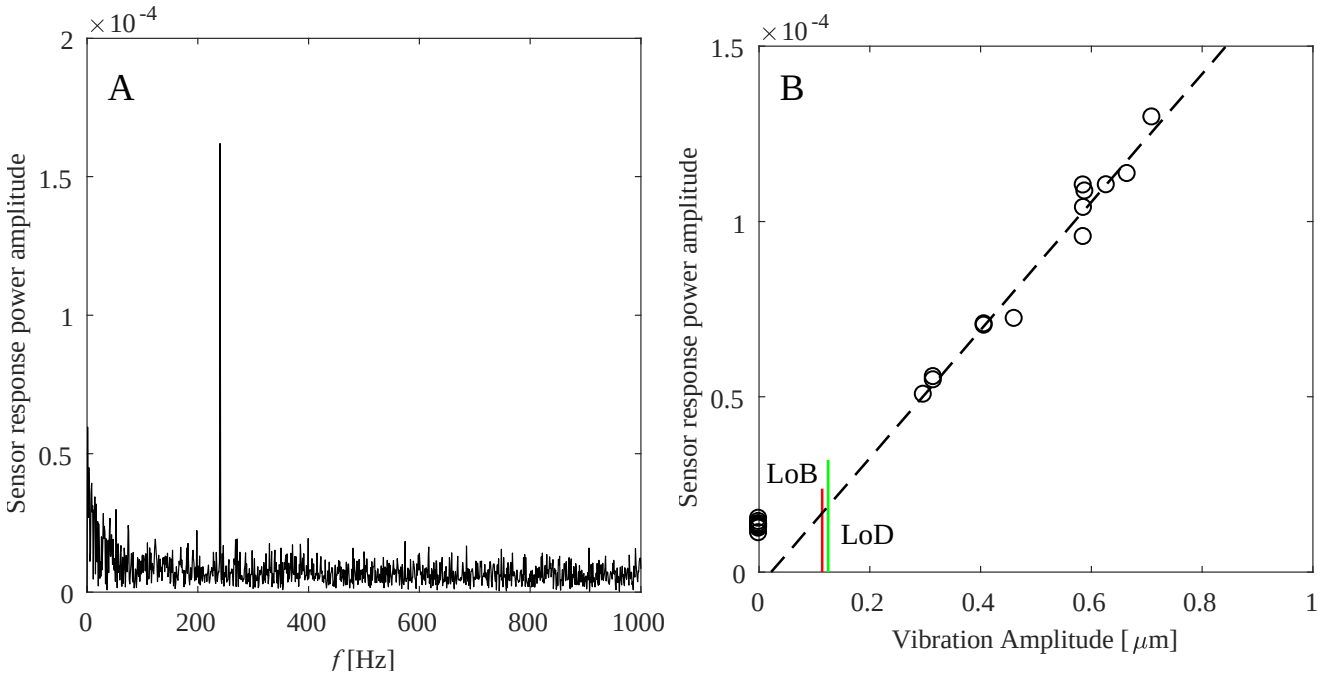

Figure 7.10 Normal force sensor response in controlled vibration tests. (A) Example FFT graph of normal force sensor at 240 Hz; (B) Example calibration plot of sensor response power amplitude with respect to LDV measured vibration amplitude. Limit of detection (LoD) is defined in the same way as section 5.3.

Figure 7.11A shows sensor response power and LDV measured vibrating displacement with respect to frequency. Both the response and LDV vibration amplitude increases to the maximum as the frequency reaches the actuating system's natural frequency at 410 Hz, then decreases as frequency continues to increase. The sensor response magnitude is above the noise floor (less than 1E-4, not shown) for frequencies below 1 kHz.

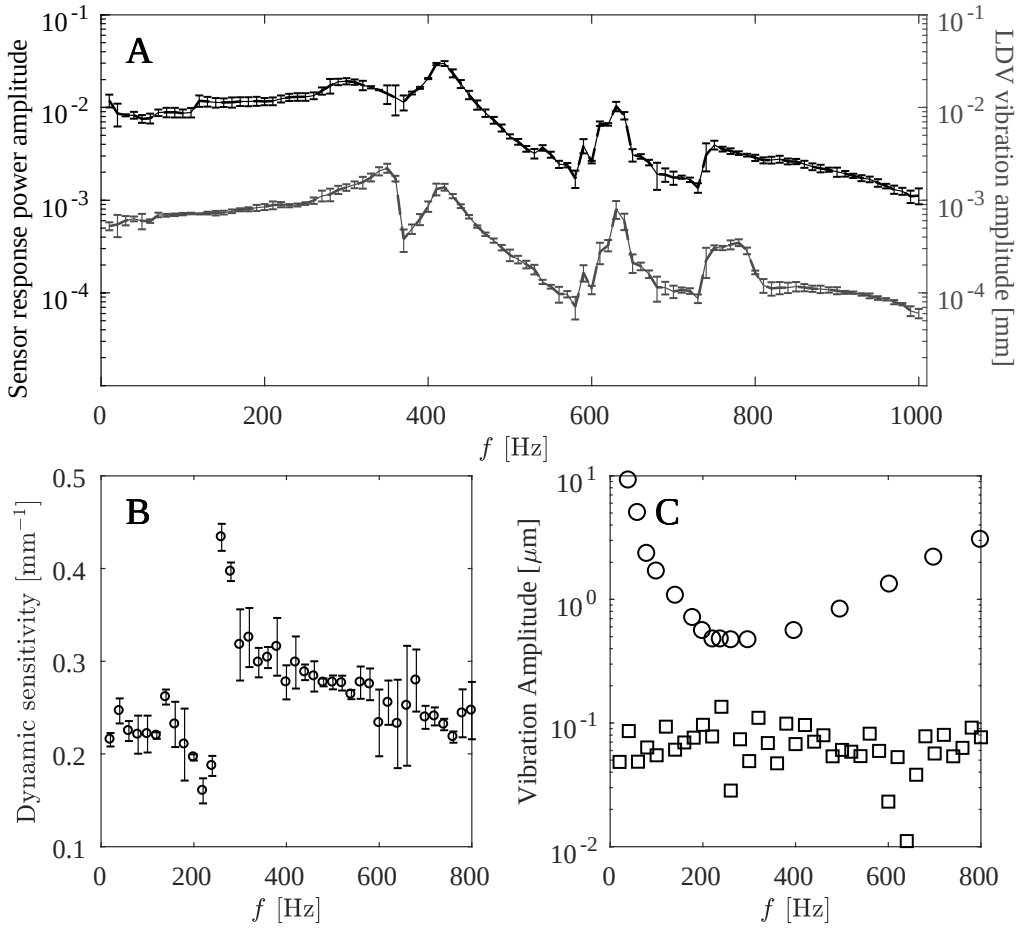

Figure 7.11 Normal force sensor response in controlled vibration tests. (A) Normal sensing taxel signal power magnitude (black line) and actuated displacement magnitude measured by LDV (grey line) at different frequencies. The sensor response closely reflects the variation of the vibration amplitude. (B) Sensor response sensitivity calculated as the slope of the calibration as in Figure 7.10A. Data was collected in 20 Hz increment. Error bars show standard deviation from 3 independent trials. The function is relatively constant up to 200 Hz, showing a primary peak around 260 Hz and rolls off after that. (C) Displacement detection threshold of shear sensing skin (squares) and human (circles) as a function of frequency. Human sensitivity data is extracted from Fishel and Loeb [16] . Sensor presented superior threshold to human up to 800 Hz by almost one order of magnitude.

Figure 7.11B shows dynamic sensitivity as the quotient of the sensor response and the vibration amplitude measured by LDV. The sensor shows relatively constant sensitivity below 200 Hz, a primary resonance at 260 Hz, and gradually rolls off until 1 kHz. Figure 7.11C shows the sensor vibration detection threshold using limit of detection and its comparison to human sensing capabilities. The sensor is superior to human vibration sensing up to 800 Hz by almost one order of magnitude. There is no large variation of the threshold, which is below a few hundred nanometers up to 800 Hz. Such vibration sensing capabilities can be expected from all normal force sensing units distributed on the fingertip.

8. Summary and Future Work

Here we report a bioinspired, thin and flexible shear force sensor skin that deforms in response to applied shear forces similar to a human fingertip. The tension and compression are measured by embedded liquid metal strain gauges that are strategically placed adjacent to the nail bed, away from the point of finger-object contact. Such arrangement avoids co-locating multiple modalities and provides unrestricted design space when developing multi-layered, continuous skins. The fingerpad skin is designed in analogous to human skin to be stretched as a continuum with little friction against the rigid fingertip. Resistive strain gauge sensors that leverage strain difference across the fingertip are strategically placed to resolve the shear force. The resistive shear sensing skin is intrinsically flexible, conformable to curved surfaces, and immune to fatigue or other problems of solid-state sensors when subjected to repeated large strains. The artificial skin requires little modification of the fingertip and is straightforward to apply to various existing end-effectors. The sensing elements are designed on the side of the fingertip embedded in a deformable elastomer. Thus it's highly applicable for curved surfaces such as robot or prosthetic fingertips.

Static finite element models and experiments, in the light touch regime, predict a linear sensor response that is independent of the applied normal force. The resistive shear sensing skin exhibits greater than 10-bit dynamic range (up to 5 N). At higher shear forces, the experiments show a nonlinear response where the sensor sensitivity increases at higher shear forces. The nonlinearity observed in experiments could be captured in the simulations using a more comprehensive, three-dimensional, hyperelastic mechanical finite element model. Dynamic characterization including stepwise unloading, slip tests and controlled vibration revealed that the sensor is capable of capturing dynamic shear force, providing tactile cues to insipient slip and

the measurement of vibration reaching human sensing capabilities of 0.43 μm up to 800 Hz. We demonstrated the sensor's performance on a robotic manipulator during pick and place, release, and handoff tests. The sensor response indicated tactile events and proved to provide useful tactile information of finger-object interaction as well as object-world interaction.

The design is further expanded to a multi-modal sensing skin with 8 normal force sensing taxels and 4 shear force sensing strain gauges. By adding additional strain gauges shear force could be resolved in two dimensions. The normal force sensor is developed to fit the sensor skin that is designed to be mounted on a plastic fingertip. The skin sensor provided dispersed normal force information with a force resolution of 5 mN. The normal force sensor is shown to be 10-bit in resolution and little cross-talk is found. Shear force sensors reported monotonic response with sensitivity of 4.7 %/N and 3.2 %/N. The shear force sensor can be characterized as a 9-bit sensor, yet its sensitivity needs to be improved and recommendations of increasing skin flexibility and reducing orthogonal direction skin tab effect are proposed. Vibration sensing capabilities of the normal force sensors showed that it's capable of measuring vibrating displacement of less than 20 nm up to 1 kHz.

Throughout this work the reported maximum force is approximately 5 N. However, the shear sensor skin or the integrated sensor skin is capable of measuring 8 N from observation of a failure test. Characterization of these sensors at higher force levels would yield better understanding of the non-linear behavior that is observed. A failure analysis and cycled strain experiment would better illustrate the robustness of the soft flexible sensor skin to repeated large strain.

The high frequency actuating system used to evaluate the vibration sensing has natural frequencies in the bandwidth of interest and resulted in unreliable measurement around these frequencies. Since natural frequency is proportional to $\sqrt{stiffness/mass}$, it can be raised by increasing stiffness or reducing mass. Thus the measurement under 1 kHz would characterize the sensor's vibration sensing capabilities with more confidence.

There is room of improvement for the integrated sensor skin. The normal force sensor can be further miniaturized to allow for higher spatial resolution. The shear sensor taxels suffers from insufficient sensitivity for light touch and this weakness can be addressed in a few ways. The finger might be modified so that the minimum radius of curvature is increased for better conformal wrapping. The reservoirs can be moved further behind the mounting brackets so that it is no longer necessary to increase the skin thickness at the position where radius of curvature is small. The four tabs connecting to the center of the skin can be designed such that they are soft to shear displacement but stiff to tensile displacement using modified geometry or anisotropic material. Thus for a given shear displacement, tabs of orthogonal direction will generate less reaction forces, concentrating the strain to the co-linear tabs and increasing sensor sensitivity. One proposal is to create softened region as shown in Figure 8.1. Additionally, surface treatment has to be implemented so that the friction coefficient between the PDMS skin and the core can be greatly reduced.

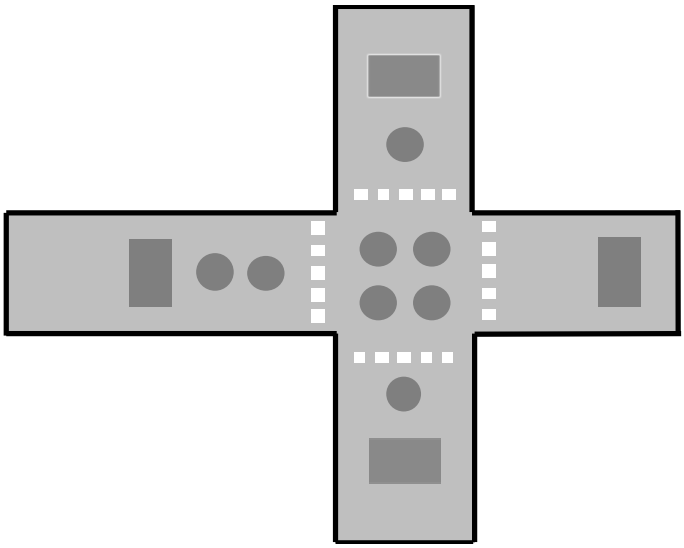

Figure 8.1 Future design of the skin pattern. Dark grey areas are normal and shear force sensor locations; white squares represent punched holes that reduce local stiffness of the skin. Another approach is to use anisotropic material at the white square location that has low shear modulus but is strong in the direction of tension, for example using fibers.

A major constraint in the current channel dimension design is PDMS handling technique and syringe filling requirements. With better channel filling technologies the sensor microchannel dimension can be further reduced and yield better performance. The sensor skin design could be further improved such that it is more robust to the environment. The flexible lead wires could be moved to a more secured area to reduce accidental contact and undesired stress. The skin pattern could be redesigned to fully cover the fingertip to keep the skin-finger interface properties constant. The advantages of the integrated sensor skin can be explored by examining the sensor performance on robotic fingertip during manipulating tasks. With the ability to resolve contact force in three dimensions, the integrated sensor would provide more tactile information in tasks involving contact, grip, stroke and texture recognition.

The demonstration of a multi-modal sensing skin calls for a fully sensorized finger with modular sensing skin mounted on different phalanges. It has been shown that a modular sensor-embedded glove can be fabricated integrating sensing taxels into a finger glove [68]. The sensing performance requirement might be relaxed on the proximal part, yet the increasing number of sensors and lead wires would soon justify the need of data acquisition at the hand. A microcontroller on the finger along with amplifying circuit could read the sensor and transmit signals to a controlling computer via wireless, I2C, serial or USB connection.

Since the shear force sensor and the multi-modal sensing skin have demonstrated potential to detect tactile events such as slip, a feedback control loop can be implemented for low-level fast reflex reaction without user intervention such as preventing slip. A decision can be made base on the tactile information collected from the multi-modal sensing skin to adjust the grip force to prevent slip or delicate object damage. With both normal and shear sensing modalities as well as vibration sensing capabilities, now the controller can also find coefficient of friction or recognize texture through sliding exploratory motion.

The skin is the largest organ of humans. The robot's ability to interact with the surroundings is greatly supported by tactile sensing. Human tactile sensing capability is the gold standard of the sensor field. The need for sensitive, expansive tactile sensors of large dynamic range is still unmet. This work presents one potential pathway for sensing skin that is bio-inspired idea and leverages existing soft-lithography technology and pushes it to its current edge to accommodate normal and shear force sensing taxels in the constrained geometry of an artificial fingertip. This work is one of few studies that demonstrate its vibration sensing capabilities and usefulness on robotic manipulator application.

Tactile sensing is slowly shifting from measuring traditionally defined terms such as force and pressure towards application specific cues such as occurrence of tactile events. These tactile cues may serve better input to machine learning type algorithms. It takes time to train sensing algorithms similar to humans that take years to learn to manipulate objects with high dexterity. Robot autonomy requires advancement of both the tactile sensors that acquire information and algorithm that interprets it.

Reference

[1] A. W. Goodwin and H. E. Wheat, “Sensory Signals in Neural Populations Underlying Tactile Perception and Manipulation,” *Annu. Rev. Neurosci.*, vol. 27, no. 1, pp. 53–77, 2004.

[2] R. S. Dahiya and M. Valle, “Human Tactile Sensing,” in *Robotic Tactile Sensing*, Springer Netherlands, 2013, pp. 19–41.

[3] R. L. Klatzky and S. J. Lederman, “Touch,” in *Handbook of Psychology, Experimental Psychology*, vol. 4, John Wiley & Sons, 2003, pp. 147–176.

[4] E. Kandel, J. Schwartz, T. Jessell, S. Siegelbaum, and A. J. Hudspeth, *Principles of Neural Science, Fifth Edition*. McGraw Hill Professional, 2012.

[5] J. M. Wolfe *et al.*, *Sensation & Perception*. Sinauer Associates, 2006.

[6] J. Dargahi and S. Najarian, “Human tactile perception as a standard for artificial tactile sensing—a review,” *Int. J. Med. Robot.*, vol. 1, no. 1, pp. 23–35, Jun. 2004.

[7] M. Gentilucci, I. Toni, E. Daprati, and M. Gangitano, “Tactile input of the hand and the control of reaching to grasp movements,” *Exp. Brain Res.*, vol. 114, no. 1, pp. 130–137, Mar. 1997.

[8] P. Gysin, T. R. Kaminski, and A. M. Gordon, “Coordination of fingertip forces in object transport during locomotion,” *Exp. Brain Res.*, vol. 149, no. 3, pp. 371–379, Feb. 2003.

[9] G. Westling and D. R. S. Johansson, “Factors influencing the force control during precision grip,” *Exp. Brain Res.*, vol. 53, no. 2, pp. 277–284, Jan. 1984.

[10] S. J. Bensmaia, P. V. Denchev, J. F. Dammann, J. C. Craig, and S. S. Hsiao, “The Representation of Stimulus Orientation in the Early Stages of Somatosensory Processing,” *J. Neurosci.*, vol. 28, no. 3, pp. 776–786, Jan. 2008.

[11] M. E. H. Eltaib and J. R. Hewit, “Tactile sensing technology for minimal access surgery—a review,” *Mechatronics*, vol. 13, no. 10, pp. 1163–1177, Dec. 2003.

[12] R. S. Johansson and J. R. Flanagan, “Coding and use of tactile signals from the fingertips in object manipulation tasks,” *Nat. Rev. Neurosci.*, vol. 10, no. 5, pp. 345–359, May 2009.

[13] J. R. Flanagan and A. M. Wing, “The Role of Internal Models in Motion Planning and Control: Evidence from Grip Force Adjustments during Movements of Hand-Held Loads,” *J. Neurosci.*, vol. 17, no. 4, pp. 1519–1528, Feb. 1997.

[14] A. M. Smith, C. E. Chapman, M. Deslandes, J.-S. Langlais, and M.-P. Thibodeau, “Role of friction and tangential force variation in the subjective scaling of tactile roughness,” *Exp. Brain Res.*, vol. 144, no. 2, pp. 211–223, Mar. 2002.

[15] J. A. Fishel and G. E. Loeb, “Bayesian Exploration for Intelligent Identification of Textures,” *Front. Neurorobotics*, vol. 6, Jun. 2012.

[16] J. A. Fishel and G. E. Loeb, “Sensing tactile microvibrations with the BioTac — Comparison with human sensitivity,” in *2012 4th IEEE RAS EMBS International Conference on Biomedical Robotics and Biomechatronics (BioRob)*, 2012, pp. 1122–1127.

[17] J. Scheibert, S. Leurent, A. Prevost, and G. Debrégeas, “The Role of Fingerprints in the Coding of Tactile Information Probed with a Biomimetic Sensor,” *Science*, vol. 323, no. 5920, pp. 1503–1506, Mar. 2009.

[18] R. Fagiani, F. Massi, E. Chatelet, Y. Berthier, and A. Akay, “Tactile perception by friction induced vibrations,” *Tribol. Int.*, vol. 44, no. 10, pp. 1100–1110, Sep. 2011.

[19] H. Zahouani, S. Mezghani, R. Vargiolu, T. Hoc, and M. EL Mansori, “Effect of roughness on vibration of human finger during a friction test,” *Wear*, vol. 301, no. 1–2, pp. 343–352, Apr. 2013.
[20] A. B. Vallbo and R. S. Johansson, “Properties of cutaneous mechanoreceptors in the human hand related to touch sensation,” *Hum. Neurobiol.*, vol. 3, no. 1, pp. 3–14, 1984.
[21] K. O. Johnson, T. Yoshioka, and F. Vega-Bermudez, “Tactile Functions of Mechanoreceptive Afferents Innervating the Hand:,” *J. Clin. Neurophysiol.*, vol. 17, no. 6, pp. 539–558, Nov. 2000.
[22] K. O. Johnson, “The roles and functions of cutaneous mechanoreceptors,” *Curr. Opin. Neurobiol.*, vol. 11, no. 4, pp. 455–461, Aug. 2001.
[23] S. J. B. Jr, G. A. Gescheider, R. T. Verrillo, and C. M. Checkosky, “Four channels mediate the mechanical aspects of touch,” *J. Acoust. Soc. Am.*, vol. 84, no. 5, pp. 1680–1694, Nov. 1988.
[24] H. Olausson, J. Wessberg, and N. Kakuda, “Tactile directional sensibility: peripheral neural mechanisms in man,” *Brain Res.*, vol. 866, no. 1–2, pp. 178–187, Jun. 2000.
[25] B. B. Edin and N. Johansson, “Skin strain patterns provide kinaesthetic information to the human central nervous system.,” *J. Physiol.*, vol. 487, no. 1, pp. 243–251, Aug. 1995.
[26] D. F. Collins and A. Prochazka, “Movement illusions evoked by ensemble cutaneous input from the dorsum of the human hand.,” *J. Physiol.*, vol. 496, no. Pt 3, pp. 857–871, Nov. 1996.
[27] “Somatosensation - Neuroscience | Fastbleep.” [Online]. Available: http://www.fastbleep.com/biology-notes/39/145/911. [Accessed: 11-May-2016].
[28] R. S. Dahiya, G. Metta, M. Valle, and G. Sandini, “Tactile sensing—from humans to humanoids,” *Robot. IEEE Trans. On*, vol. 26, no. 1, pp. 1–20, 2010.
[29] K. S. Hale and K. M. Stanney, “Deriving haptic design guidelines from human physiological, psychophysical, and neurological foundations,” *IEEE Comput. Graph. Appl.*, vol. 24, no. 2, pp. 33–39, Mar. 2004.
[30] J. Monzée, Y. Lamarre, and A. M. Smith, “The Effects of Digital Anesthesia on Force Control Using a Precision Grip,” *J. Neurophysiol.*, vol. 89, no. 2, pp. 672–683, Feb. 2003.
[31] B. Preising, T. C. Hsia, and B. Mittelstadt, “A literature review: robots in medicine,” *IEEE Eng. Med. Biol. Mag.*, vol. 10, no. 2, pp. 13–22, Jun. 1991.
[32] B. Gates, “A Robot in Every Home,” *Sci. Am.*, vol. 18, pp. 4–11, 2008.
[33] K. Ziegler-Graham, E. J. MacKenzie, P. L. Ephraim, T. G. Travison, and R. Brookmeyer, “Estimating the Prevalence of Limb Loss in the United States: 2005 to 2050,” *Arch. Phys. Med. Rehabil.*, vol. 89, no. 3, pp. 422–429, Mar. 2008.
[34] A. Saikia *et al.*, “Recent advancements in prosthetic hand technology,” *J. Med. Eng. Technol.*, vol. 0, no. 0, pp. 1–10, Apr. 2016.
[35] E. A. Biddiss and T. T. Chau, “Upper limb prosthesis use and abandonment: A survey of the last 25 years,” *Prosthet. Orthot. Int.*, vol. 31, no. 3, pp. 236–257, Jan. 2007.
[36] M. A. James, A. M. Bagley, K. Brasington, C. Lutz, S. McConnell, and F. Molitor, “Impact of Prostheses on Function and Quality of Life for Children with Unilateral Congenital Below-the-Elbow Deficiency,” *J. Bone Jt. Surg.*, vol. 88, no. 11, pp. 2356–2365, Nov. 2006.
[37] E. A. Biddiss and T. T. Chau, “Multivariate prediction of upper limb prosthesis acceptance or rejection,” *Disabil. Rehabil. Assist. Technol.*, vol. 3, no. 4, pp. 181–192, Jan. 2008.

[38] R. D. Ponce Wong, R. B. Hellman, and V. J. Santos, "Spatial Asymmetry in Tactile Sensor Skin Deformation Aids Perception of Edge Orientation During Haptic Exploration," *IEEE Trans. Haptics*, vol. 7, no. 2, pp. 191–202, Apr. 2014.

[39] M. I. Tiwana, S. J. Redmond, and N. H. Lovell, "A review of tactile sensing technologies with applications in biomedical engineering," *Sens. Actuators Phys.*, vol. 179, pp. 17–31, 2012.

[40] Johan Tegin and Jan Wikander, "Tactile sensing in intelligent robotic manipulation – a review," *Ind. Robot Int. J.*, vol. 32, no. 1, pp. 64–70, Feb. 2005.

[41] N. Chen, R. Rink, and H. Zhang, "Efficient edge detection from tactile data," in *1995 IEEE/RSJ International Conference on Intelligent Robots and Systems 95. 'Human Robot Interaction and Cooperative Robots', Proceedings*, 1995, vol. 3, pp. 386–391 vol.3.

[42] C. Muthukrishnan, D. Smith, D. Myers, J. Rebman, and A. Koivo, "Edge detection in tactile images," in *1987 IEEE International Conference on Robotics and Automation. Proceedings*, 1987, vol. 4, pp. 1500–1505.

[43] H. Yousef, M. Boukallel, and K. Althoefer, "Tactile sensing for dexterous in-hand manipulation in robotics—A review," *Sens. Actuators Phys.*, vol. 167, no. 2, pp. 171–187, 2011.

[44] R. Howe and M. Cutkosky, "Sensing skin acceleration for slip and texture perception," in , *1989 IEEE International Conference on Robotics and Automation, 1989. Proceedings*, 1989, pp. 145–150 vol.1.

[45] Z. Su *et al.*, "Force estimation and slip detection/classification for grip control using a biomimetic tactile sensor," in *2015 IEEE-RAS 15th International Conference on Humanoid Robots (Humanoids)*, 2015, pp. 297–303.

[46] Z. Su, J. A. Fishel, T. Yamamoto, and G. E. Loeb, "Use of tactile feedback to control exploratory movements to characterize object compliance," *Front. Neurorobotics*, vol. 6, Jul. 2012.

[47] J. Reinecke, A. Dietrich, F. Schmidt, and M. Chalon, "Experimental comparison of slip detection strategies by tactile sensing with the BioTac® on the DLR hand arm system," in *2014 IEEE International Conference on Robotics and Automation (ICRA)*, 2014, pp. 2742–2748.

[48] R. S. Johansson and J. R. Flanagan, "Tactile Sensory Control of Object Manipulation in Humans," in *The Senses: A Comprehensive Reference*, R. H. Masland, T. D. Albright, T. D. Albright, R. H. Masland, P. Dallos, D. Oertel, S. Firestein, G. K. Beauchamp, M. C. Bushnell, A. I. Basbaum, J. H. Kaas, and E. P. Gardner, Eds. New York: Academic Press, 2008, pp. 67–86.

[49] S. P. Patarinski and R. G. Botev, "Robot force control: A review," *Mechatronics*, vol. 3, no. 4, pp. 377–398, Aug. 1993.

[50] M. R. Tremblay and M. R. Cutkosky, "Estimating friction using incipient slip sensing during a manipulation task," in , *1993 IEEE International Conference on Robotics and Automation, 1993. Proceedings*, 1993, pp. 429–434 vol.1.

[51] H. Zhao, K. O'Brien, S. Li, and R. F. Shepherd, "Optoelectronically innervated soft prosthetic hand via stretchable optical waveguides," *Sci. Robot.*, vol. 1, no. 1, p. eaai7529, Dec. 2016.

[52] M. Sohgawa *et al.*, "Tactile array sensor with inclined chromium/silicon piezoresistive cantilevers embedded in elastomer," in *TRANSDUCERS 2009 - 2009 International Solid-State Sensors, Actuators and Microsystems Conference*, 2009, pp. 284–287.

[53] H. B. Muhammad *et al.*, “A capacitive tactile sensor array for surface texture discrimination,” *Microelectron. Eng.*, vol. 88, no. 8, pp. 1811–1813, Aug. 2011.
[54] H. B. Muhammad *et al.*, “Development of a bioinspired MEMS based capacitive tactile sensor for a robotic finger,” *Sens. Actuators Phys.*, vol. 165, no. 2, pp. 221–229, Feb. 2011.
[55] A. Wisitsoraat, V. Patthanasetakul, T. Lomas, and A. Tuantranont, “Low cost thin film based piezoresistive MEMS tactile sensor,” *Sens. Actuators Phys.*, vol. 139, no. 1–2, pp. 17–22, Sep. 2007.
[56] A. Bicchi and V. Kumar, “Robotic grasping and contact: a review,” in *IEEE International Conference on Robotics and Automation, 2000. Proceedings. ICRA ’00*, 2000, vol. 1, pp. 348–353 vol.1.
[57] P. Peng, R. Rajamani, and A. G. Erdman, “Flexible Tactile Sensor for Tissue Elasticity Measurements,” *J. Microelectromechanical Syst.*, vol. 18, no. 6, pp. 1226–1233, Dec. 2009.
[58] H.-K. Lee, J. Chung, S.-I. Chang, and E. Yoon, “Normal and Shear Force Measurement Using a Flexible Polymer Tactile Sensor With Embedded Multiple Capacitors,” *J. Microelectromechanical Syst.*, vol. 17, no. 4, pp. 934–942, Aug. 2008.
[59] H. K. Lee, S. I. Chang, and E. Yoon, “A Flexible Polymer Tactile Sensor: Fabrication and Modular Expandability for Large Area Deployment,” *J. Microelectromechanical Syst.*, vol. 15, no. 6, pp. 1681–1686, Dec. 2006.
[60] J.-H. Park, J.-H. An, Y.-J. Kim, Y.-H. Huh, and H.-J. Lee, “Tensile and high cycle fatigue test of copper thin film,” *Mater. Werkst.*, vol. 39, no. 2, pp. 187–192, Feb. 2008.
[61] T. Ando, M. Shikida, and K. Sato, “Tensile-mode fatigue testing of silicon films as structural materials for MEMS,” *Sens. Actuators Phys.*, vol. 93, no. 1, pp. 70–75, Aug. 2001.
[62] J. Bagdahn and W. N. Sharpe Jr., “Fatigue of polycrystalline silicon under long-term cyclic loading,” *Sens. Actuators Phys.*, vol. 103, no. 1–2, pp. 9–15, Jan. 2003.
[63] R. D. Ponce Wong, R. B. Hellman, and V. J. Santos, “Haptic exploration of fingertip-sized geometric features using a multimodal tactile sensor,” presented at the SPIE Sensing Technology+ Applications. International Society for Optics and Photonics, 2014.
[64] N. Wettels, V. J. Santos, R. S. Johansson, and G. E. Loeb, “Biomimetic Tactile Sensor Array,” *Adv. Robot.*, vol. 22, no. 8, pp. 829–849, Jan. 2008.
[65] R. D. Ponce Wong, J. D. Posner, and V. J. Santos, “Flexible microfluidic normal force sensor skin for tactile feedback,” *Sens. Actuators Phys.*, vol. 179, pp. 62–69, 2012.
[66] M. L. Hammock, A. Chortos, B. C.-K. Tee, J. B.-H. Tok, and Z. Bao, “25th Anniversary Article: The Evolution of Electronic Skin (E-Skin): A Brief History, Design Considerations, and Recent Progress,” *Adv. Mater.*, vol. 25, no. 42, pp. 5997–6038, Nov. 2013.
[67] F. L. Hammond, R. K. Kramer, Q. Wan, R. D. Howe, and R. J. Wood, “Soft Tactile Sensor Arrays for Force Feedback in Micromanipulation,” *IEEE Sens. J.*, vol. 14, no. 5, pp. 1443–1452, May 2014.
[68] F. L. Hammond, Y. Menguc, and R. J. Wood, “Toward a modular soft sensor-embedded glove for human hand motion and tactile pressure measurement,” in *Intelligent Robots and Systems (IROS 2014), 2014 IEEE/RSJ International Conference on*, 2014, pp. 4000–4007.
[69] M. T. Francomano, D. Accoto, and E. Guglielmelli, “Artificial Sense of Slip - A Review,” *IEEE Sens. J.*, vol. 13, no. 7, pp. 2489–2498, Jul. 2013.

[70] S. Chitta, J. Sturm, M. Piccoli, and W. Burgard, "Tactile Sensing for Mobile Manipulation," *IEEE Trans. Robot.*, vol. 27, no. 3, pp. 558–568, Jun. 2011.
[71] Y.-L. Park, C. Majidi, R. Kramer, P. Bérard, and R. J. Wood, "Hyperelastic pressure sensing with a liquid-embedded elastomer," *J. Micromechanics Microengineering*, vol. 20, no. 12, p. 125029, 2010.
[72] P. Roberts, D. D. Damian, W. Shan, T. Lu, and C. Majidi, "Soft-matter capacitive sensor for measuring shear and pressure deformation," in *2013 IEEE International Conference on Robotics and Automation (ICRA)*, 2013, pp. 3529–3534.
[73] D. M. Vogt, Y.-L. Park, and R. J. Wood, "Design and Characterization of a Soft Multi-Axis Force Sensor Using Embedded Microfluidic Channels," *IEEE Sens. J.*, vol. 13, no. 10, pp. 4056–4064, Oct. 2013.
[74] C. Majidi, R. Kramer, and R. J. Wood, "A non-differential elastomer curvature sensor for softer-than-skin electronics," *Smart Mater. Struct.*, vol. 20, no. 10, p. 105017, 2011.
[75] Y.-L. Park, B.-R. Chen, and R. J. Wood, "Design and Fabrication of Soft Artificial Skin Using Embedded Microchannels and Liquid Conductors," *IEEE Sens. J.*, vol. 12, no. 8, pp. 2711–2718, Aug. 2012.
[76] Y.-J. Yang *et al.*, "An integrated flexible temperature and tactile sensing array using PI-copper films," *Sens. Actuators Phys.*, vol. 143, no. 1, pp. 143–153, May 2008.
[77] F. Schneider, T. Fellner, J. Wilde, and U. Wallrabe, "Mechanical properties of silicones for MEMS," *J. Micromechanics Microengineering*, vol. 18, no. 6, p. 065008, 2008.
[78] F. L. Hammond, R. K. Kramer, Q. Wan, R. D. Howe, and R. J. Wood, "Soft tactile sensor arrays for micromanipulation," in *2012 IEEE/RSJ International Conference on Intelligent Robots and Systems (IROS)*, 2012, pp. 25–32.
[79] W. Merlijn van Spengen, "MEMS reliability from a failure mechanisms perspective," *Microelectron. Reliab.*, vol. 43, no. 7, pp. 1049–1060, Jul. 2003.
[80] S. Stassi, V. Cauda, G. Canavese, and C. F. Pirri, "Flexible Tactile Sensing Based on Piezoresistive Composites: A Review," *Sensors*, vol. 14, no. 3, pp. 5296–5332, Mar. 2014.
[81] A. Charalambides and S. Bergbreiter, "A novel all-elastomer MEMS tactile sensor for high dynamic range shear and normal force sensing," *J. Micromechanics Microengineering*, vol. 25, no. 9, p. 095009, 2015.
[82] J. Engel, J. Chen, N. Chen, S. Pandya, and C. Liu, "Multi-Walled Carbon Nanotube Filled Conductive Elastomers: Materials and Application to Micro Transducers," in *19th IEEE International Conference on Micro Electro Mechanical Systems*, 2006, pp. 246–249.
[83] B. Zhu *et al.*, "Microstructured Graphene Arrays for Highly Sensitive Flexible Tactile Sensors," *Small*, vol. 10, no. 18, pp. 3625–3631, Sep. 2014.
[84] T. Lu, L. Finkenauer, J. Wissman, and C. Majidi, "Rapid Prototyping for Soft-Matter Electronics," *Adv. Funct. Mater.*, vol. 24, no. 22, pp. 3351–3356, Jun. 2014.
[85] M. D. Dickey, R. C. Chiechi, R. J. Larsen, E. A. Weiss, D. A. Weitz, and G. M. Whitesides, "Eutectic Gallium-Indium (EGaIn): A Liquid Metal Alloy for the Formation of Stable Structures in Microchannels at Room Temperature," *Adv. Funct. Mater.*, vol. 18, no. 7, pp. 1097–1104, 2008.
[86] K. Doudrick *et al.*, "Different Shades of Oxide: From Nanoscale Wetting Mechanisms to Contact Printing of Gallium-Based Liquid Metals," *Langmuir*, vol. 30, no. 23, pp. 6867–6877, Jun. 2014.
[87] C. Ladd, J.-H. So, J. Muth, and M. D. Dickey, "3D Printing of Free Standing Liquid Metal Microstructures," *Adv. Mater.*, vol. 25, no. 36, pp. 5081–5085, Sep. 2013.

[88] L. Wang and J. Liu, “Liquid Metal Inks for Flexible Electronics and 3D Printing: A Review,” presented at the ASME 2014 International Mechanical Engineering Congress and Exposition. American Society of Mechanical Engineers, 2014.

[89] J. Wissman, T. Lu, and C. Majidi, “Soft-matter electronics with stencil lithography,” in *2013 IEEE SENSORS*, 2013, pp. 1–4.

[90] L. Viry *et al.*, “Flexible Three-Axial Force Sensor for Soft and Highly Sensitive Artificial Touch,” *Adv. Mater.*, vol. 26, no. 17, pp. 2659–2664, May 2014.

[91] M. Weigel, T. Lu, G. Bailly, A. Oulasvirta, C. Majidi, and J. Steimle, “iSkin: Flexible, Stretchable and Visually Customizable On-Body Touch Sensors for Mobile Computing,” in *Proceedings of the 33rd Annual ACM Conference on Human Factors in Computing Systems*, New York, NY, USA, 2015, pp. 2991–3000.

[92] K. Noda, K. Hoshino, K. Matsumoto, and I. Shimoyama, “A shear stress sensor for tactile sensing with the piezoresistive cantilever standing in elastic material,” *Sens. Actuators Phys.*, vol. 127, no. 2, pp. 295–301, Mar. 2006.

[93] A. Drimus, G. Kootstra, A. Bilberg, and D. Kragic, “Design of a flexible tactile sensor for classification of rigid and deformable objects,” *Robot. Auton. Syst.*, vol. 62, no. 1, pp. 3–15, Jan. 2014.

[94] J. Yin, V. J. Santos, and J. D. Posner, “Bioinspired Flexible Microfluidic Shear Force Sensor Skin,” *Sens. Actuators Phys.*, in press.

[95] E. S. Hwang, J. h Seo, and Y. J. Kim, “A Polymer-Based Flexible Tactile Sensor for Both Normal and Shear Load Detections and Its Application for Robotics,” *J. Microelectromechanical Syst.*, vol. 16, no. 3, pp. 556–563, Jun. 2007.

[96] J. Dargahi, M. Parameswaran, and S. Payandeh, “A micromachined piezoelectric tactile sensor for an endoscopic grasper-theory, fabrication and experiments,” *J. Microelectromechanical Syst.*, vol. 9, no. 3, pp. 329–335, Sep. 2000.

[97] J. i Yuji and C. Sonoda, “A PVDF Tactile Sensor for Static Contact Force and Contact Temperature,” in *2006 5th IEEE Conference on Sensors*, 2006, pp. 738–741.

[98] E. S. Kolesar, R. R. Reston, D. G. Ford, and R. C. Fitch, “Multiplexed piezoelectric polymer tactile sensor,” *J. Robot. Syst.*, vol. 9, no. 1, pp. 37–63, Feb. 1992.

[99] E. S. Kolesar, C. S. Dyson, R. R. Reston, R. C. Fitch, D. G. Ford, and S. D. Nelms, “Tactile integrated circuit sensor realized with a piezoelectric polymer,” in , *Eighth Annual IEEE International Conference on Innovative Systems in Silicon, 1996. Proceedings*, 1996, pp. 372–381.

[100] N. Futai, N. Futai, K. Matsumoto, and I. Shimoyama, “A flexible micromachined planar spiral inductor for use as an artificial tactile mechanoreceptor,” *Sens. Actuators Phys.*, vol. 111, no. 2–3, pp. 293–303, Mar. 2004.

[101] S. Takenawa, “A soft three-axis tactile sensor based on electromagnetic induction,” in *IEEE International Conference on Mechatronics, 2009. ICM 2009*, 2009, pp. 1–6.

[102] X. Chen, S. Yang, M. Hasegawa, K. Takeuchi, K. Kawabe, and S. Motojima, “Novel Tactile Sensors Manufactured by Carbon Microcoils,” in *2004 International Conference on MEMS, NANO and Smart Systems, 2004. ICMENS 2004. Proceedings*, 2004, pp. 486–491.

[103] M. Ohka, Y. Mitsuya, I. Higashioka, and H. Kabeshita, “An Experimental Optical Three-axis Tactile Sensor for Micro-Robots,” *Robotica*, vol. 23, no. 04, pp. 457–465, Jul. 2005.

[104] M. Ohka, N. Morisawa, H. Suzuki, J. Takata, H. Koboyashi, and H. B. Yussof, "A robotic finger equipped with an optical three-axis tactile sensor," in *IEEE International Conference on Robotics and Automation, 2008. ICRA 2008*, 2008, pp. 3425–3430.
[105] E. Cheung and V. Lumelsky, "A sensitive skin system for motion control of robot arm manipulators," *Robot. Auton. Syst.*, vol. 10, no. 1, pp. 9–32, Jan. 1992.
[106] M. Ohka, Y. Mitsuya, Y. Matsunaga, and S. Takeuchi, "Sensing characteristics of an optical three-axis tactile sensor under combined loading," *Robotica*, vol. 22, no. 02, pp. 213–221, Mar. 2004.
[107] H. Yussof, M. Ohka, H. Kobayashi, J. Takata, M. Yamano, and Y. Nasu, "Development of an Optical Three-Axis Tactile Sensor for Object Handing Tasks in Humanoid Robot Navigation System," in *Autonomous Robots and Agents*, D. S. C. Mukhopadhyay and G. S. Gupta, Eds. Springer Berlin Heidelberg, 2007, pp. 43–51.
[108] M. Ohka, H. Kobayashi, J. Takata, and Y. Mitsuya, "Sensing Precision of an Optical Three-axis Tactile Sensor for a Robotic Finger," in *ROMAN 2006 - The 15th IEEE International Symposium on Robot and Human Interactive Communication*, 2006, pp. 214–219.
[109] M. A. Qasaimeh*, S. Sokhanvar, J. Dargahi, and M. Kahrizi, "PVDF-Based Microfabricated Tactile Sensor for Minimally Invasive Surgery," *J. Microelectromechanical Syst.*, vol. 18, no. 1, pp. 195–207, Feb. 2009.
[110] S. Sokhanvar, M. Packirisamy, and J. Dargahi, "A multifunctional PVDF-based tactile sensor for minimally invasive surgery," *Smart Mater. Struct.*, vol. 16, no. 4, p. 989, 2007.
[111] G. F. B. I. Baumann P. K.Plinkert, W.Kunert, "Vibrotactile characteristics of different tissues in endoscopic otolaryngologic surgery - in vivo and ex vivo measurements," *Minim. Invasive Ther. Allied Technol.*, vol. 10, no. 6, pp. 323–327, Jan. 2001.
[112] E. Petter, M. Biehl, and J. U. Meyer, "Vibrotactile palpation instrument for use in minimal invasive surgery," in *Proceedings of the 18th Annual International Conference of the IEEE Engineering in Medicine and Biology Society, 1996. Bridging Disciplines for Biomedicine*, 1996, vol. 1, pp. 179–180 vol.1.
[113] G. M. Krishna and K. Rajanna, "Tactile sensor based on piezoelectric resonance," *IEEE Sens. J.*, vol. 4, no. 5, pp. 691–697, Oct. 2004.
[114] S. Ando and H. Shinoda, "Ultrasonic emission tactile sensing," *IEEE Control Syst.*, vol. 15, no. 1, pp. 61–69, Feb. 1995.
[115] Y. Yamada and M. R. Cutkosky, "Tactile sensor with 3-axis force and vibration sensing functions and its application to detect rotational slip," in *1994 IEEE International Conference on Robotics and Automation*, 1994, pp. 3550–3557 vol.4.
[116] P. Puangmali, K. Althoefer, L. D. Seneviratne, D. Murphy, and P. Dasgupta, "State-of-the-Art in Force and Tactile Sensing for Minimally Invasive Surgery," *IEEE Sens. J.*, vol. 8, no. 4, pp. 371–381, Apr. 2008.
[117] A. M. Okamura, "Haptic Feedback in Robot-Assisted Minimally Invasive Surgery," *Curr. Opin. Urol.*, vol. 19, no. 1, pp. 102–107, Jan. 2009.
[118] J. W. Boley, E. L. White, G. T.-C. Chiu, and R. K. Kramer, "Direct Writing of Gallium-Indium Alloy for Stretchable Electronics," *Adv. Funct. Mater.*, vol. 24, no. 23, pp. 3501–3507, Jun. 2014.
[119] I. D. Johnston, D. K. McCluskey, C. K. L. Tan, and M. C. Tracey, "Mechanical characterization of bulk Sylgard 184 for microfluidics and microengineering," *J. Micromechanics Microengineering*, vol. 24, no. 3, p. 035017, 2014.

[120] V. N. Parthasarathy, C. M. Graichen, and A. F. Hathaway, “A comparison of tetrahedron quality measures,” *Finite Elem. Anal. Des.*, vol. 15, no. 3, pp. 255–261, Jan. 1994.
[121] M. Meyer, R. M. Kirby, and R. Whitaker, “Topology, Accuracy, and Quality of Isosurface Meshes Using Dynamic Particles,” *IEEE Trans. Vis. Comput. Graph.*, vol. 13, no. 6, pp. 1704–1711, Nov. 2007.
[122] J. Shewchuk, “What is a good linear finite element? interpolation, conditioning, anisotropy, and quality measures (preprint),” *Univ. Calif. Berkeley*, vol. 73, 2002.
[123] S. Yu and M. Kaviany, “Electrical, thermal, and species transport properties of liquid eutectic Ga-In and Ga-In-Sn from first principles,” *J. Chem. Phys.*, vol. 140, no. 6, p. 064303, Feb. 2014.
[124] B. E. Schubert and D. Floreano, “Variable stiffness material based on rigid low-melting-point-alloy microstructures embedded in soft poly(dimethylsiloxane) (PDMS),” *RSC Adv.*, vol. 3, no. 46, pp. 24671–24679, Nov. 2013.
[125] J. Yin, P. Aspinall, V. J. Santos, and J. D. Posner, “Measuring Dynamic Shear Force and Vibration with a Bioinspired Tactile Sensor Skin,” Submitted.
[126] H. Yoshizawa and J. Israelachvili, “Fundamental mechanisms of interfacial friction. 2. Stick-slip friction of spherical and chain molecules,” *J. Phys. Chem.*, vol. 97, no. 43, pp. 11300–11313, Oct. 1993.
[127] M. D. Borysiak, M. J. Thompson, and J. D. Posner, “Translating diagnostic assays from the laboratory to the clinic: analytical and clinical metrics for device development and evaluation,” *Lab. Chip*, vol. 16, no. 8, pp. 1293–1313, Apr. 2016.
[128] S. Bistac, M. Schmitt, and A. Ghorbal, “Sliding Friction of Polymers: The Complex Role of Interface,” in *Fundamentals of Friction and Wear*, D. E. Gnecco and P. D. E. Meyer, Eds. Springer Berlin Heidelberg, 2007, pp. 647–658.
[129] W. Townsend, “The BarrettHand grasper – programmably flexible part handling and assembly,” *Ind. Robot Int. J.*, vol. 27, no. 3, pp. 181–188, Jun. 2000.